AFRL-RI-RS-TR-2022-057

INTEGRATED QUANTUM PHOTONICS FOR PHOTON-ION ENTANGLEMENT

ROCHESTER INSTITUTE OF TECHNOLOGY

APRIL 2022

FINAL TECHNICAL REPORT

APPROVED FOR PUBLIC RELEASE; DISTRIBUTION UNLIMITED

STINFO COPY

AIR FORCE RESEARCH LABORATORY
INFORMATION DIRECTORATE

■ **AIR FORCE MATERIEL COMMAND** ■ **UNITED STATES AIR FORCE** ■ **ROME, NY 13441**

NOTICE AND SIGNATURE PAGE

Using Government drawings, specifications, or other data included in this document for any purpose other than Government procurement does not in any way obligate the U.S. Government. The fact that the Government formulated or supplied the drawings, specifications, or other data does not license the holder or any other person or corporation; or convey any rights or permission to manufacture, use, or sell any patented invention that may relate to them.

This report is the result of contracted fundamental research deemed exempt from public affairs security and policy review in accordance with SAF/AQR memorandum dated 10 Dec 08 and AFRL/CA policy clarification memorandum dated 16 Jan 09. This report is available to the general public, including foreign nations. Copies may be obtained from the Defense Technical Information Center (DTIC) (http://www.dtic.mil).

AFRL-RI-RS-TR-2022-057 HAS BEEN REVIEWED AND IS APPROVED FOR PUBLICATION IN ACCORDANCE WITH ASSIGNED DISTRIBUTION STATEMENT.

FOR THE CHIEF ENGINEER:

/ S /
JON M. MAGGIOLINO
Work Unit Manager

/ S /
GREGORY J. HADYNSKI
Assistant Technical Advisor
Computing & Communications Division
Information Directorate

This report is published in the interest of scientific and technical information exchange, and its publication does not constitute the Government's approval or disapproval of its ideas or findings.

REPORT DOCUMENTATION PAGE

1. REPORT DATE	2. REPORT TYPE	3. DATES COVERED	
		START DATE	END DATE
APRIL 2022	FINAL TECHNICAL REPORT	MARCH 2016	SEPTEMBER 2021

4. TITLE AND SUBTITLE

INTEGRATED QUANTUM PHOTONICS FOR PHOTON-ION ENTANGLEMENT

5a. CONTRACT NUMBER	5b. GRANT NUMBER	5c. PROGRAM ELEMENT NUMBER
FA8750-16-2-0140	N/A	62788F

5d. PROJECT NUMBER	5e. TASK NUMBER	5f. WORK UNIT NUMBER
		R1XQ

6. AUTHOR(S)

Stefan F. Preble

7. PERFORMING ORGANIZATION NAME(S) AND ADDRESS(ES)

Rochester Institute of Technology
1 Lomb Memorial Drive
Rochester NY 14623

8. PERFORMING ORGANIZATION REPORT NUMBER

9. SPONSORING/MONITORING AGENCY NAME(S) AND ADDRESS(ES)	10. SPONSOR/MONITOR'S ACRONYM(S)	11. SPONSOR/MONITOR'S REPORT NUMBER(S)
Air Force Research Laboratory/RITQ 525 Brooks Road Rome NY 13441-4505	RI	AFRL-RI-RS-TR-2022-057

12. DISTRIBUTION/AVAILABILITY STATEMENT

Approved for Public Release; Distribution Unlimited. This report is the result of contracted fundamental research deemed exempt from public affairs security and policy review in accordance with SAF/AQR memorandum dated 10 Dec 08 and AFRL/CA policy clarification memorandum dated 16 Jan 09.

13. SUPPLEMENTARY NOTES

14. ABSTRACT

This project focused on the realization of an integrated platform for quantum photonics. Photonic Integrated Circuit (PIC) technologies enable the integration of all the components of a quantum photonic system (photon sources, interferometers for manipulating the photon state) onto a high density, phase stable, high efficiency, and high-performance Silicon substrate. However, traditional PIC fabrication has been optimized for classical applications where loss and crosstalk are not as important. In this project we worked with AFRL and AIM Photonics to successfully realize a foundry quantum integrated platform, along with the key device and circuit level building blocks (photon sources, low loss waveguides, interferometers, phase shifters). We also demonstrated robust optical and electrical packaging that enables the chips to be interfaced with optical fiber networks and electrical hardware.

15. SUBJECT TERMS

Integrated Quantum Photonics, Photonic Integrated Circuits, Foundry, Photon Sources, Quantum Information

16. SECURITY CLASSIFICATION OF:			17. LIMITATION OF ABSTRACT	18. NUMBER OF PAGES
a. REPORT	b. ABSTRACT	C. THIS PAGE		
U	U	U	SAR	44

19a. NAME OF RESPONSIBLE PERSON	19b. PHONE NUMBER *(Include area code)*
JON M. MAGGIOLINO	N/A

PREVIOUS EDITION IS OBSOLETE.

TABLE OF CONTENTS

LIST OF FIGURES

1.0 SUMMARY

This project focused on the realization of an integrated platform for quantum photonics. Photonic Integrated Circuit (PIC) technologies enable the integration of all the components of a quantum photonic system (photon sources, interferometers for manipulating the photon state) onto a high density, phase stable, high efficiency, and high-performance Silicon substrate. However, traditional PIC fabrication has been optimized for classical applications where loss and crosstalk are not as important. In this project we worked with AFRL and AIM Photonics to successfully realize a foundry quantum integrated platform, along with the key device and circuit level building blocks (photon sources, low loss waveguides, interferometers, phase shifters). We also demonstrated robust optical and electrical packaging that enables the chips to be interfaced with optical fiber networks and electrical hardware.

2.0 INTRODUCTION

Quantum integrated photonics leverages semiconductor manufacturing to realize scalable, phase stable, integration of sources of entangled photons and circuits to manipulate their quantum states. This approach has delivered significant demonstrations of quantum computing [1], quantum communication [2] and quantum simulation [3]. Furthermore, chip-scale fabrication enables the hybrid integration of solid state emitters [4], nonlinear/electro-optic materials [5] and single photon detectors [6]; and the integration of quantum photonic devices with other qubit platforms, including, superconductors [7] and ions [8].

In this collaborative project with AFRL, we developed the first foundry fabricated quantum integrated photonics platforms, taking our initial research from the university cleanroom to the AIM Photonics foundry. We completed multi-project-wafer (MPW) runs to demonstrate the initial building blocks and then realized DoD's first 300mm Quantum Photonic Wafer. The wafer process is optimized for quantum, with the first demonstration of low loss Silicon and Silicon Nitride waveguides (<0.5dB/cm) in a fully active process [9]. These low losses enable quantum circuits that generate bright entangled photons and manipulate entanglement robustly. Building on this, in 2021 we completed the tape-out of a second 300mm Quantum Photonic Wafer which further increases quantum functionalities with dopants optimized for active quantum photonic devices (electro-optic modulators and switches), and trenches for: micro-electro-mechanical (MEMS) phase shifters that operate with ultra-low voltages [10] and are cryogenically compatible; photonic wirebonds for low loss coupling to fibers and lasers; and hybrid integration with solid state quantum emitters, electro-optic polymers, nonlinear materials and single photon detectors. The chips are also designed for robust packaging, with integration to fiber arrays and dense electrical interconnects.

This report summarizes the project and its development of a foundry integrated quantum photonic platform. Specifically, we describe the key building blocks, such as, photon sources with high brightness and efficiency; the approach to pump separation; low-loss circuits for manipulating photon entanglement, including a novel approach for realizing Hong-Ou-Mandel (HOM) in a quantum ring resonator; the phase shifters for controlling the photon interference in

quantum PICs; and robust photonic + electrical packaging which will ultimately enable these quantum PICs to be deployed in future systems.

3.0 METHODS, ASSUMPTIONS, AND PROCEDURES

3.1 Quantum Integrated Photonic Platform

We have developed, in collaboration with AFRL/RITQ and AIM Photonics, a quantum photonic wafer platform based on 300mm Silicon wafers (Figure 1). Silicon Quantum Photonics leverages CMOS foundry manufacturing to realize high performance passive and active photonic devices based on Silicon and Silicon Nitride (SiN) waveguides. This platform has all the materials (Silicon, SiN, Germanium, Metals) and doping's for realizing a full suite of tunable devices, including, photon sources, phase shifters, electro-optic modulators, attenuators, switches, and photodetectors. The 300mm foundry manufacturing available at AIM Photonics enables the high yield, reproducibility, and performance necessary for realizing complex quantum photonic circuits. However, quantum photonics requires enhancements and optimizations to a standard silicon photonic process to enable robust photon generation and processing. We have developed such a quantum photonic wafer platform with an initial wafer run (Fig. 1(a)) consisting of the key building blocks and in 2021 a second wafer design (Fig. 1(b)). The key elements of this quantum integrated photonic platform are the following:

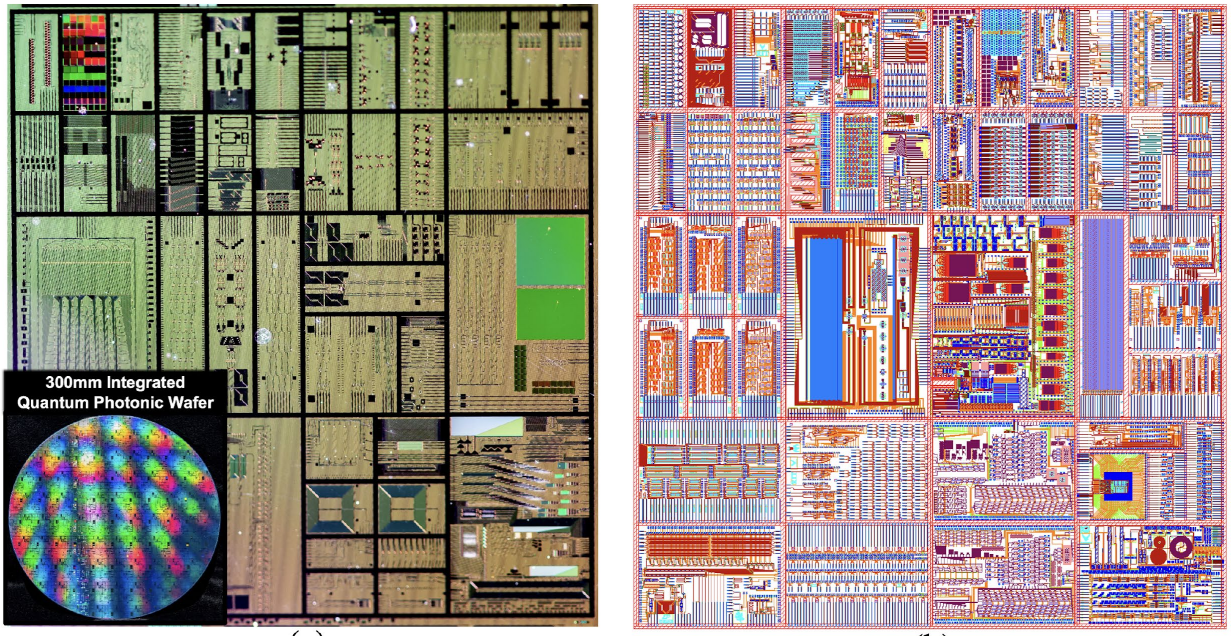

Figure 1: Quantum Integrated Photonic Platforms (a) DoD's first 300mm integrated quantum photonic wafer (Photos Credit: M. Fanto and C. Tison, AFRL/RITQ). The wafer was fabricated by AIM Photonics. The wafer fabrication was optimized for low loss, low noise Silicon and SiN waveguides, and fiber-to-chip coupling. (b) 2021 AFRL 300mm Quantum Photonic Wafer reticle design with active electro-optic process and devices optimized for quantum photonic applications. The wafer also has trenches for realizing Micro-electro-mechanical (MEMs) devices, efficient

thermo-optic modulation and hybrid integration of electro-optic polymers, single photon emitters, heterogeneous materials and superconducting nanowire detectors.

- Low loss Silicon (<0.5dB/cm) and SiN (<0.25dB/cm) single mode strip waveguides were demonstrated [9]. These are critical for the generation, routing, and manipulation of single photons.
- High purity waveguide materials to ensure that photon noise from defects in the Silicon oxide and Silicon nitride is minimized. AIM Photonics implemented annealing processes to purify the materials.
- Low dispersion waveguides that enable phase matching of nonlinear optical processes
- SMF28 Edge Couplers with a coupling loss of <1dB has been demonstrated (Figure 21).
- Doping profiles and levels optimized for active quantum photonic devices that enable low loss modulation and switching, while achieving high bandwidths needed for flying qubits and quantum frequency processing. The dopings also enable other active devices, including, phase shifters, and electric-field profiles for interacting with quantum emitters and nonlinear materials.
- Trenches that expose the Silicon and Silicon Nitride waveguides for:
    - Photonic wire bonds for low loss coupling to fibers and lasers using two-photon lithography processing [11]
    - Micro-electro Mechanical (MEMs) sacrificial release trenches that enable low voltage, cryogenically compatible, phase shifting [10,12]
    - Solid state emitters that can be integrated directly with Silicon/SiN waveguides and optical cavities [4]
    - Modulators that utilize hybrid integration of organic materials or nonlinear optical materials [13]
    - Photodetectors that can detect single photons, such as, superconducting nanowires [6]

These quantum wafers (Fig. 1(a&b)) include test structures for evaluating wafer performance, and quantum devices/circuits that implement: photon sources, high dimensional entanglement, quantum neural networks, quantum frequency processors, and programmable unitaries for linear quantum optical computing.

3.2 Photon Sources

Quantum photonics requires bright sources of single photons. The sources must be scalable and tunable to integrate them together and optimize their performance for maximal entanglement. Silicon waveguides are a highly promising source of photon pairs (Figure 2). It has a large third-order nonlinearity, and the large index-contrast (n_{Si}=3.5, n_{SiO2}=1.45) creates a highly confined optical mode (Fig. 2) which maximizes that nonlinearity. Furthermore, standard singlemode 500×220nm Silicon-on-Insulator Waveguides have low group velocity dispersion (zero or slightly anomalous), enabling the phase matching of the spontaneous four wave mixing (SFWM) process. Using a milliwatt level pump laser, coupled into centimeter long waveguides, non-degenerate signal/idler photon pairs can be produced at high rates. Alternatively, degenerate biphotons can be produced with two pump lasers tuned to the blue/red of the biphoton wavelength, as depicted in Figure 2.

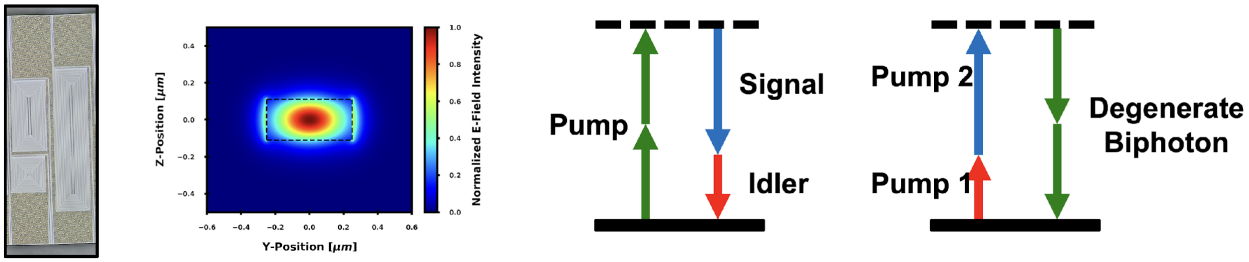

Figure 2: Silicon Waveguide Photon Sources. Spontaneous four wave mixing (SFWM) in Silicon waveguides enables the generation of non-degenerate (signal/idler at different frequencies) or degenerate photon pairs. The strong confinement of the optical mode yields a high generation rate.

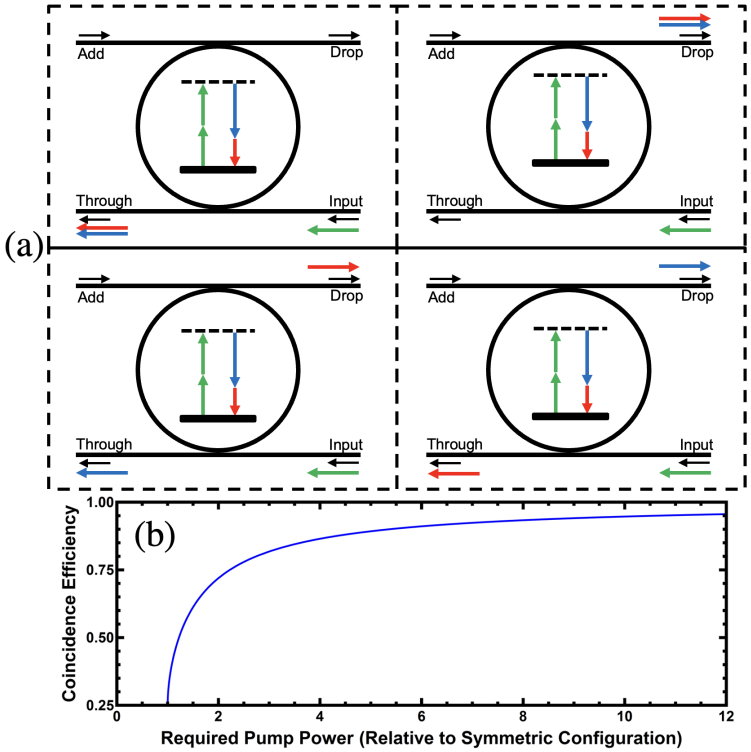

Figure 3: Ring Resonator Photon Source Tradeoffs (a) Ring resonators suffer from a tradeoff where the generated photon pairs (red/blue arrows) can exit the ring resonator through four possibilities, resulting in a 25% chance both photons exit the intended port. (b) The ring resonator can be engineered to direct the photons only out the drop port, increasing the coincidence efficiency at that port, but it requires asymptotically approaching infinite pump powers.

Resonators are commonly used to enhance the spectral brightness of the photon pairs. Specifically, the bandwidth of the resonator will dictate the bandwidth of the generated photon pairs. In the past several years, significant advances in high performance resonant photon sources have been made using nonlinear photon generation in Silicon resonators using (SFWM) [14–20]. Resonators meet the requirements of providing scalability (they are very compact) and tunability. However, in this project we found that there is a tradeoff between the sources brightness and the probability that the photons will exit the resonator without being lost (heralding efficiency) [20–

23]. The tradeoff exists because the resonator must be critically coupled to maximize the pump laser intensity inside the ring, but this comes at the cost that on 25% of the pair will end up at the desired port even though their rate of production is at its highest (Fig. 3(a) [21].

We investigated this tradeoff [21] and found that in practice the optical loss of the pump can be traded off for a dramatic increase in heralding/coincidence efficiency. Specifically, a critically coupled ring resonator requires both the input/drop port waveguides to have the same gap (symmetric configuration – assuming the loss of the ring is negligible compared to the coupling strengths). This symmetric configuration maximizes the pump power in the ring resonator, but the generated photon pairs can leave the resonator in four different ways (Fig. 3(a)). By increasing the gap between the input waveguide (used to pump the resonator) and the ring, the coincidence efficiency can be significantly improved at the cost of pump power coupled into the ring. With a ~10× increase in the pump power, to achieve the same brightness as a standard symmetric ring resonator device, the coincidence/heralding efficiency can be improved by ~3.75× to 93.75% (from 25% for a symmetric device – Figure 3 (b)) [21]. We experimentally verified this in Section 4.1.

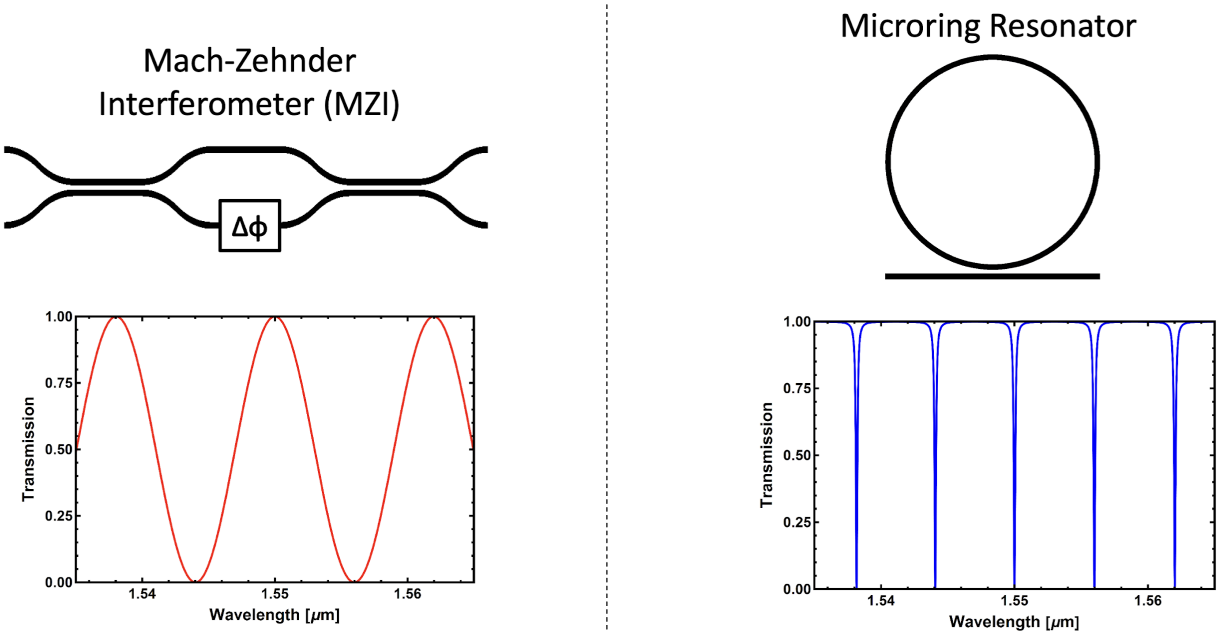

Figure 4: Towards the perfect photon source. Combining a Mach-Zehnder Interferometer (MZI) with a microring resonator enables a perfect photon source. The periodic interference of the MZI is used to control the coupling to specific ring resonances.

We now look at this tradeoff from the pump lasers and generated photons perspectives. From the pump's perspective, the ring resonator should be (1) Critically Coupled to ensure the pump is fully coupled into the resonator, (2) High-Q to get the highest intensity in the resonator and, (3) single-bus to minimize the loss (to maximize the Q). However, from the photon pairs perspective, the ring resonator should be (1) Over-coupled to ensure that the photons exit the resonator at a rate higher than they are lost within the resonator itself and, (2) single-bus to ensure the photons only exit the one port. So, how can a ring resonator be both critically coupled with a high-Q and over coupled with a low-Q simultaneously? The solution is to combine a ring resonator with another standard integrated photonic device – a Mach-Zehnder Interferometer (Figure 4).

The perfect resonant photon source, which overcomes the tradeoff by combining MZI and microring, is seen in Figure 5. The photon source interferometrically couples the ring resonator using a multipoint coupler [20,22]. This allows the coupling to the resonances to be tailored separately for the pump laser, which requires critical coupling, and the photon pairs which should be overcoupled to ensure that they exit the resonator before being lost to the intrinsic loss of the ring. And, as seen in Figure 5, this is achieved simultaneously with one interferometer at the top of the ring for pumping (MZI1), and another interferometer at the bottom tuned for the photon pairs (MZI2). This method of coupling allows resonances supported by the ring to be suppressed by the coupler. By choosing the optical path length between coupling points such that the interference pattern has a period that is twice the free spectral range of the microring, half of the resonances can be suppressed. And the second MZI is designed to have an additional π phase shift within the coupler, so that the two sides of the device become decoupled from each other. In this configuration, the dual bus microring resonator acts more like two single bus rings. If the wavelength of the pump photons is chosen to align with a resonance on one side of the device (Fig. 5 right) while the wavelengths of the signal and idler photons align with resonances on the opposing side, the device becomes highly directional. Furthermore, the couplers can be designed to allow the pump photons to be critically coupled to the input side (maximizing the effective nonlinearity) while the signal and idler photons can be overcoupled to the output side (ensuring that they leave the ring quickly). Using this design we demonstrated that >99.8% of the generated photon pairs exit the resonator and the pump laser is critically coupled, resulting in order of magnitude increases in the overall photon brightness (Section 4.2).

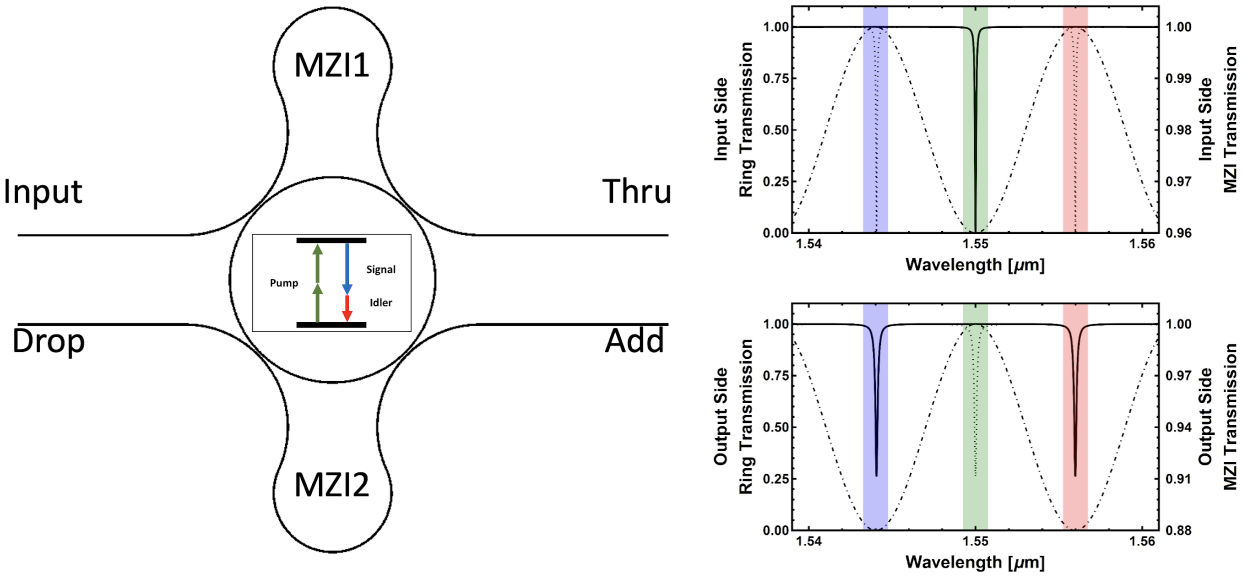

Figure 5: Interferometrically Coupled Ring Photon Source MZI1 is used to ensure that the pump is critically coupled into the ring resonator. MZI2 is used to ensure that the generated signal/idler photons exit the ring resonator only out the drop port of the resonator. The free-spectral ranges (FSR) of the two MZI's is tuned to match the resonances and decouples the input side of the resonator from the output, creating built-in pump filtering.

Under this project we have designed and realized a TM Polarized Photon Pair Source [24,25]. However, the challenge with creating a TM photon pair source is that TM polarization is highly dispersive. Consequently, it is impossible to achieve energy conservation of the nonlinear photon generation process because the resonances are not equally spaced. An approach for overcoming this is to use two independently controlled resonators that are linearly uncoupled but can be coupled through the nonlinear photon generation process [26]. Specifically, two resonators are designed to interact through a directional coupler as seen in Figure 6(a). However, the directional coupler is designed such that the net coupling between the two resonators is zero (i.e., the light couples into the second resonator and then back). Consequently, its resonances (green in Figure 6(b)) are independent of the resonances of the second resonator (red/blue in Figure 6(b)). A pair of resonances in the second resonator can be tuned such that they are equally spaced about a central resonance of the first resonator. Therefore, by using a pump laser tuned to the central green resonance, when the third-order nonlinearity of the waveguide spontaneously generates signal/idler photon pairs, energy conservation is achieved in the respective red/blue resonances. The generated photon pairs will exit the second resonator without coupling back into the first resonator as well. We demonstrated (Section 4.3) high pair generation rates and high quality heralded single photon generation using this approach [25].

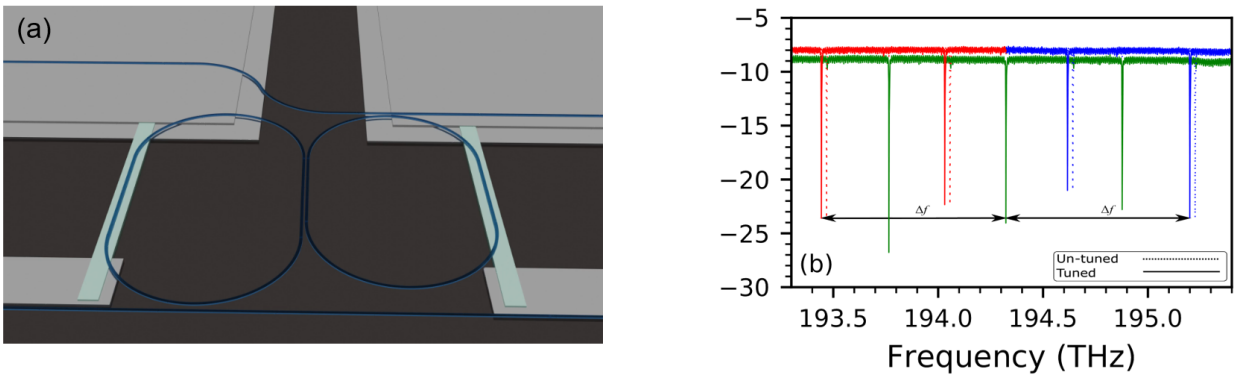

Figure 6: TM Polarized Photon Pair Source (a) Nonlinearly coupling, linearly uncoupled independent resonators (b) The two resonators can be independently tuned to select a set of resonances that allow for energy conservation of the nonlinear photon generation process.

3.3 Photon Manipulation Circuits

Quantum optical information processing generally relies on the manipulation of photons through both linear and nonlinear optical elements. This forms the basis for manipulating quantum states and entanglement, and has applications in computing, communication, and sensing. In bulk optics linear quantum optical state manipulation is achieved with phase shifting elements (wave plates) and beam splitters. The basic phenomena of two-photon interference forms the basis for quantum optical behavior of photons and is beautifully illustrated by the Hong-Ou-Mandel effect [27]. Where two indistinguishable photons are simultaneously incident on a beam splitter (Fig. 7). Photons that interfere constructively will bunch together (photon bunching), and as a result will travel together through the rest of the system (resulting in zero coincidences between

two-photon detectors at the outputs of the beam splitter). The degree which the photons are indistinguishable will determine the degree to which the photons anti-bunch, and as a result the HOM effect is a good indication of the quality of the photon source, but more importantly, lies at the heart of the proposals that enable quantum computing with single photons and linear optical elements [28].

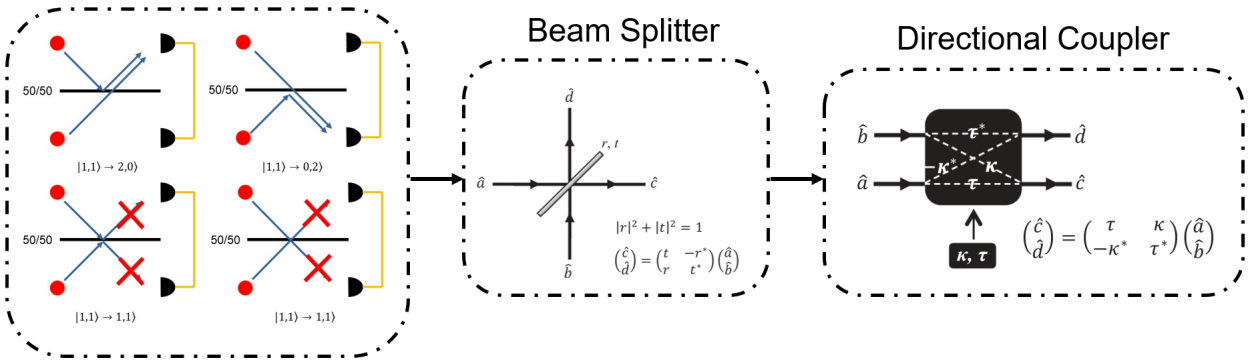

Figure 7: Hong-Ou-Mandel Effect. Identical photons incident on a beam splitter will bunch together, resulting in zero coincidences between the two detectors. The Hong-Ou-Mandel (HOM) is the basis for realizing quantum optic circuits. Directional couplers on PICs are equivalent to beam splitters.

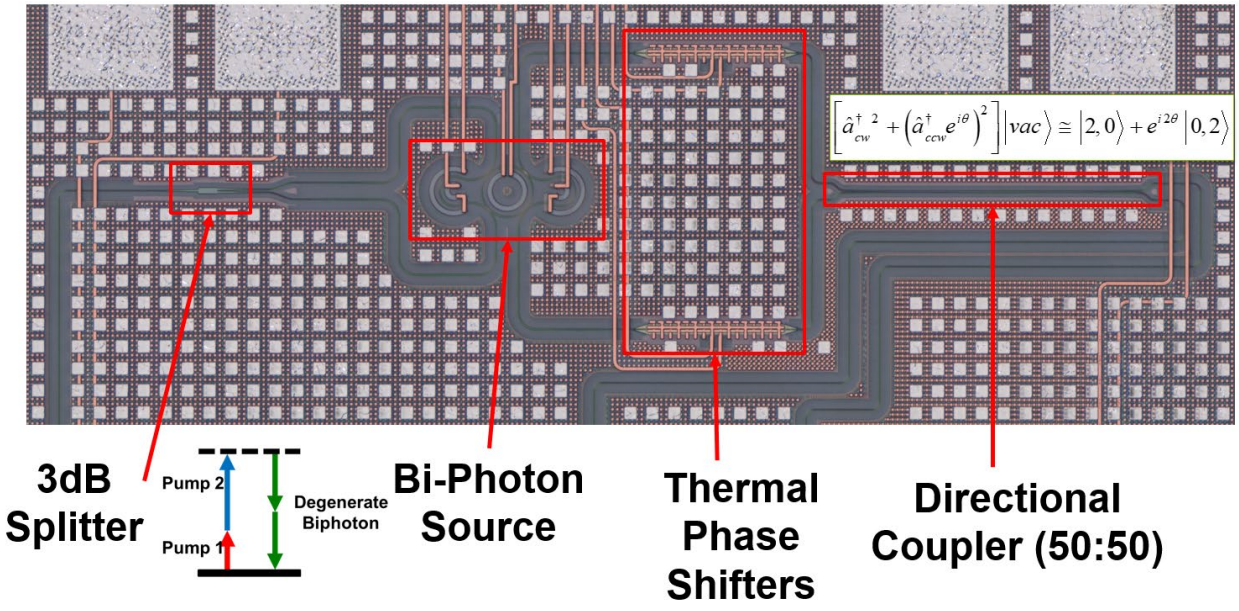

Figure 8: Two-Photon Interference on a PIC. A 3dB splitter splits two lasers, which pump a bi-photon source (interferometrically coupled ring resonator). The counter-propagating pumps produce degenerate biphotons, which are in a superposition of existing in the clockwise or counter-clockwise directions. After the biphoton exits the resonator, it passes through thermal phase shifters and then the two paths are combined on a 50:50 directional coupler. This creates two-photon interference that oscillates at 2θ.

In PICs, the directional coupler is an exact analogue to the beam splitter as depicted in Fig. 8. Specifically, it is also a 4-port device that has an effective reflectivity (κ - coupling constant) and transmission (τ). Consequently, all the theoretical basis of linear quantum optics directly applies to quantum integrated photonics and with the key advantage that photons are routed through the entire PIC circuit without the requirement for maintaining alignment and confines the photons into well controlled modes that are intrinsically phase stable. Consequently, it is straightforward to integrate photon sources directly with a directional coupler to realize the HOM effect as depicted in Figure 8. Furthermore, the phase of the photons can be controlled at will using thermal phase shifters, enabling a general demonstration of two-photon interference as we did before this project began [14].

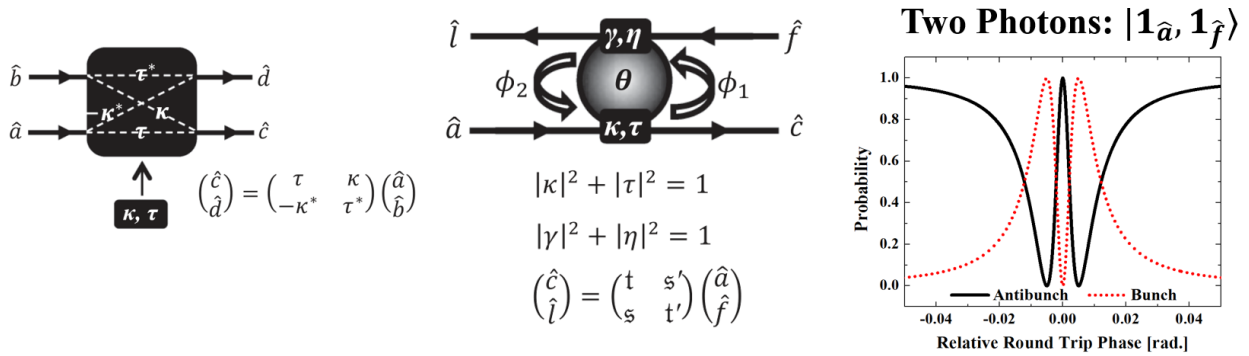

Figure 9: Quantum Ring Resonator. HOM effect requires a perfect 50:50 beam splitter / directional coupler. A ring resonator can be used to realize 50:50 coupling by simply tuning one of the operating parameters of the device (primarily phase) [29]. Consequently, perfect two-photon interference (right graph) can be achieved at an appropriate relative round trip phase.

However, while PICs dramatically reduce the size of quantum photonic circuits, the size of a directional coupler is large in comparison to the other elements of the circuit (Figure 8). In addition, HOM interference requires perfect 50:50 splitting/coupling, which is challenging to achieve because a directional coupler will only have 50:50 coupling at a single wavelength due to the intrinsic physics of the device. Consequently, we have been working to leverage ring resonators for HOM interference. Like directional couplers, as seen in Figure 9, ring resonators are also 4-port devices (that happen to internally use directional couplers to couple from the bus waveguides into the actual resonator waveguides) [29]. However, ring resonators have the key advantage that they intrinsically have a large parameter space which they can operate over. The feedback of the resonator ensures that there is a wide range of operating conditions where perfect 50:50 coupling can be achieved. Consequently, it is possible to achieve high performance HOM interference in this quantum ring resonator. An example slice of the quantum resonators space is seen in Fig. 9(c) where perfect antibunching can be achieved by selecting an appropriate roundtrip phase around the resonator.

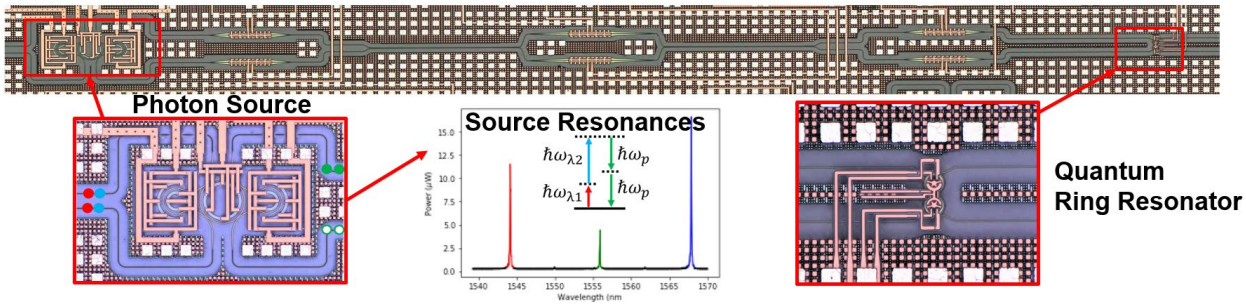

Figure 10: Quantum Ring Resonator PIC Circuit. A quantum ring resonator is integrated with a photon source, and phase shifters for preparing the quantum state.

Figure 10 features a quantum ring resonator PIC circuit experiment we completed in this project [30]. It consists of an interferometrically coupled microring photon source pumped externally by two CW telecom lasers (1.5-1.6μm) generating a spectrally degenerate biphoton (green). Photon pairs are generated clockwise and counterclockwise and launched into both arms of the photonic circuit which include a Mach-Zehnder interferometer to prepare the input states for path entanglement. Downstream, a quantum ring resonator (which uses coupled resonators to simplify the routing of the waveguides), receives and interferes the photons, producing biphoton states whose probability amplitudes can be tuned using the different thermo-optic phase shifters (Results are described in Section 4.4).

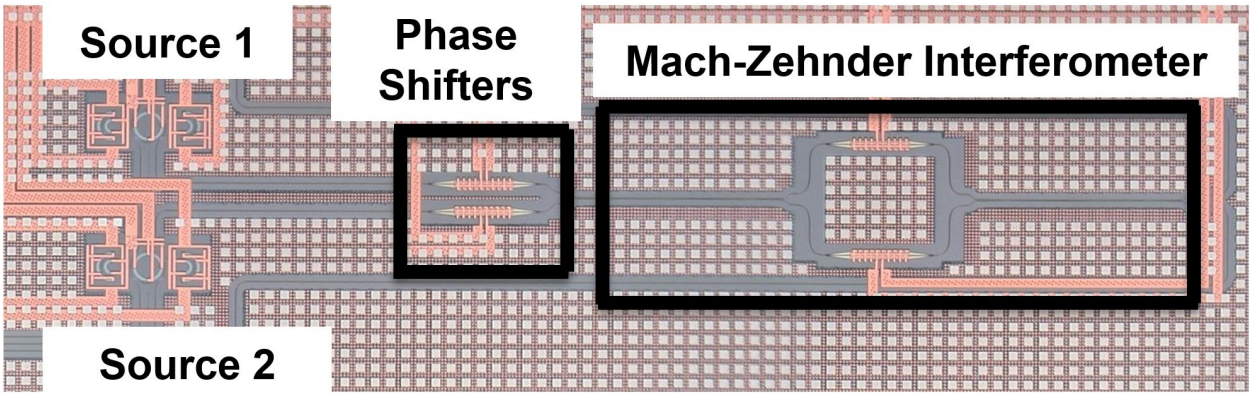

Figure 11: Two-Photon Interference from Independent Sources. Two-photon sources are pumped, and the resulting photon pairs and interfered in a Mach-Zehnder Interferometer, after state manipulation using phase shifters.

In order to scale up to larger numbers of qubits it is important to be able to interfere photons from multiple photon sources. Recently, we demonstrated interference between multiple interferometrically coupled photon sources (Fig. 11) [31]. By tuning the coupling of the pump and the out-coupling of the photons from each resonator we were able to optimize the two-photon interference visibility (>98%) between the two sources (results in Section 4.5). This is a key advantage of this photon source as any fabrication variations can be adjusted by tuning the sources coupling to ensure that the resonances are identical. This adjustability also enables the production of unentangled photon pairs [15], a key component for heralded photon sources [15,32].

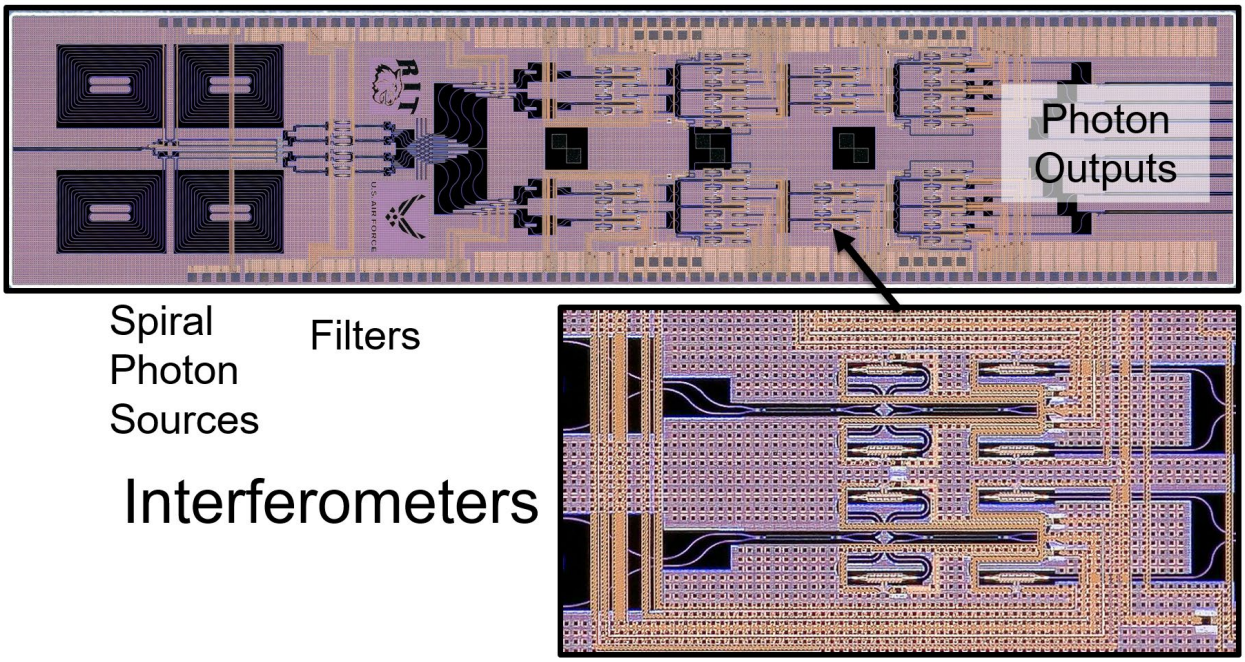

Figure 12: Quantum Programmable Processor. Arbitrary unitary operations are realized using interferometers with integrated phase shifters which provide arbitrary rotations of the quantum state. This chip integrates together spiral waveguide photon sources, with pump removal filters and multiple stages of Mach-Zehnder interferometers.

Ultimately the promise of linear optical computing relies on the practical implementation of linear operations in optical circuits. These operations form the bedrock of optical quantum information processing, wherein the circuit can manipulate quantum states of light. Recent work demonstrates a *quantum computational advantage using photons* by creating a 50-input photonic processor from bulk optic components (lenses, mirrors) with 100-output detectors and performing various experiments to demonstrate a sampling rate ~10^{14} faster than optimized supercomputers [33]. This work is groundbreaking; however, the future vision of large-scale quantum photonic computing necessitates re-engineering to an integrated solution.

Silicon photonics provides a natural path to decreasing component size while maintaining both tunability and low optical losses through the circuit. With standard silicon photonics fabrication technology, simple beam splitters and (tunable) phase shifters can be integrated directly on-chip to create arbitrarily controlled unitary operators [34]. Our work with AFRL to realize integrated quantum optical processing is seen in the example in Figure 12, which integrates spiral waveguide photon sources with a quantum programmable processor (QPP). The QPP realizes arbitrary unitary operations using a grid of Mach-Zehnder interferometers with phase shifters for realizing complete rotations of quantum states.

The challenge of realizing an integrated QPP is controlling all the phase shifters and calibrating the overall circuit. Figure 13 shows our work to package a 4x4 QPP, which consists of 10 MZI's, with 4 phase shifters each. This relatively small QPP requires 50 total electrical connections in a small footprint. In order to bridge the gap from the large PCB to the small PIC, we developed a custom fan-out Silicon interposer packaging solution in order to wire bond

effectively. After packaging we worked to calibrate the QPP circuit by developing gradient descent algorithms to route optical inputs to different outputs (Fig. 13(e)). This approach tunes each of the phase shifters (Fig. 13(d)) to reach a specific optical output function. However, with so many electrical connections it is challenging to calibrate the circuit. In particular, we found there was significant thermal crosstalk between the heater tuned phase shifters. This crosstalk impedes the ability to control the chip reliably. Consequently, we explored improved methods for phase shifting light on a PIC.

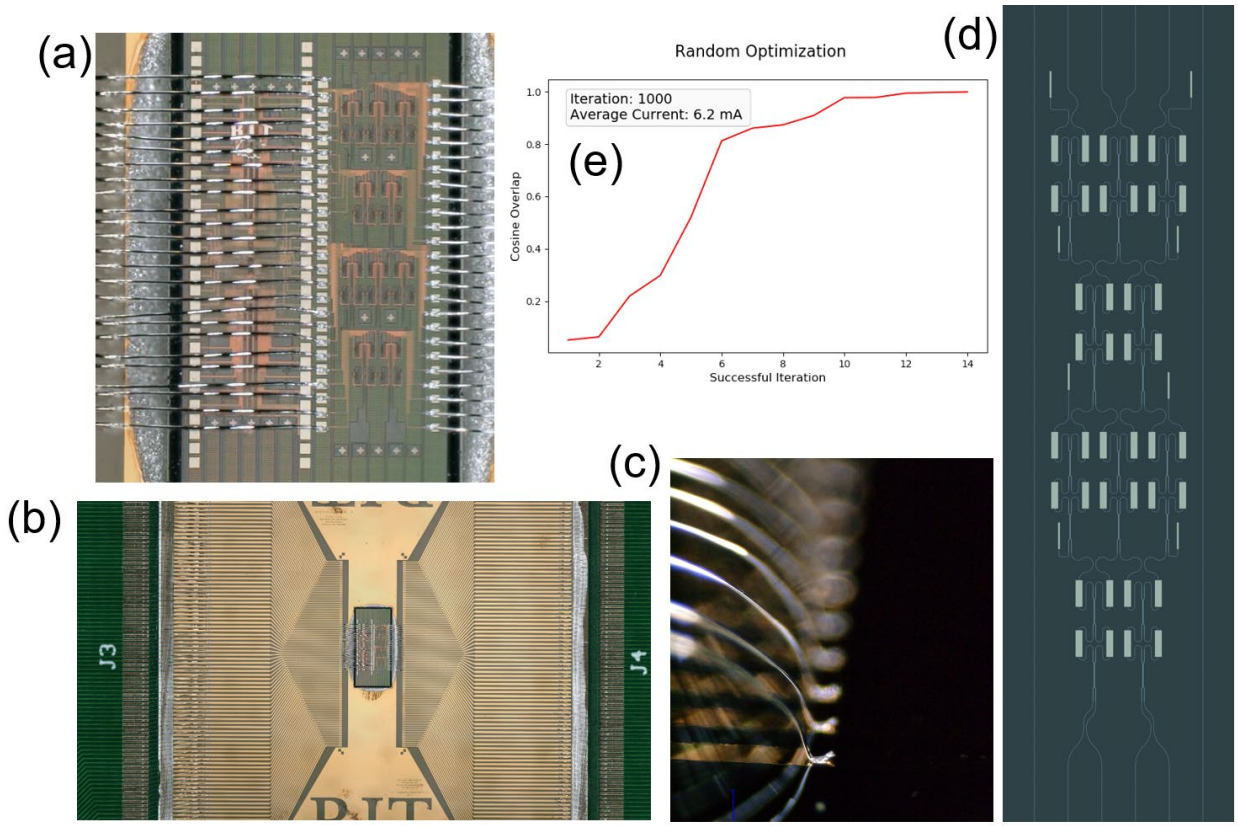

Figure 13: Packaged Quantum Programmable Processor. (a) Packaged Quantum Programmable Processor consisting of 10 MZI's (4 phase shifters each, 50 total electrical connections) (b) Zoom-out of the overall package with a RIT fabricated custom fan-out interposer (c) Zoom-in on the wire bonds. (d) Schematic of the chip design (credit: D. Starling). (e) Experimental results of the random optimization of the output of the chip to a specific output value.

Ultimately a new approach is needed for controlling photonic devices – one that does not have crosstalk and is compatible with the cryogenic operation of single photon detectors and other quantum devices. The use of Micro-Electro-Mechanical (MEMs) structures for effective index tuning of silicon-based photonic integrated circuits has evolved over recent years to reduce power consumption and maximize tuning range [35–37]. Compared to conventional thermo-optic phase shifters, MEMs-based devices, which are actuated by the electrostatic force, have proven to be power efficient, making it an ideal candidate for integrated quantum photonic applications. However, MEMs integration has historically required complex non-CMOS compatible

fabrication. Recently we proposed a new foundry-compatible silicon photonic MEMs phase shifter that utilizes gradient electric force actuation [38,39]. Gradient force actuation has recently been demonstrated in integrated photonics by Bekker et al. [37] and Pruessner et al. [35]. It operates using the fundamental principle that dielectrics experience an attractive force to strong electric fields (a typical E&M example is where a dielectric sheet is pulled into a parallel plate capacitor).

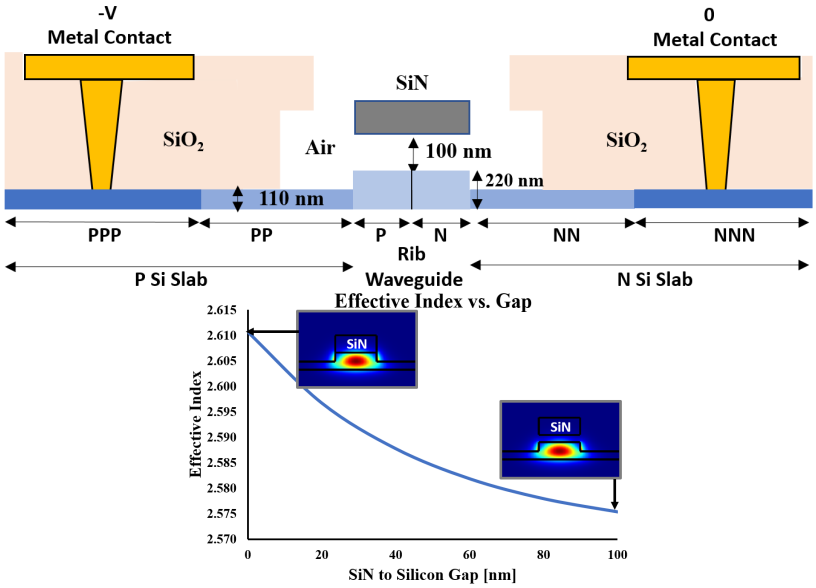

Figure 14: Ultra-Low Voltage MEMS Phase Shifter. [left] cross-sectional view of the device. [right] Effective index as the gap between the SiN and Silicon is changed. Insets show the optical modes [10,40].

The MEMs structure (silicon nitride [SiN] beam) in our device is positioned 100 nm above a PN doped silicon rib waveguide (Fig. 14[left]). Reverse biasing the silicon PN diode induces a strong electric field gradient to pull the dielectric SiN beam closer (as seen in Fig. 15) to the propagating rib waveguide mode (insets Fig. 14[right]), which induces a significant change in effective index (seen in Fig. 14[right]). This effective index change will cause a phase shift as the evanescent field of the silicon waveguide mode traverses along the silicon nitride beam's length.

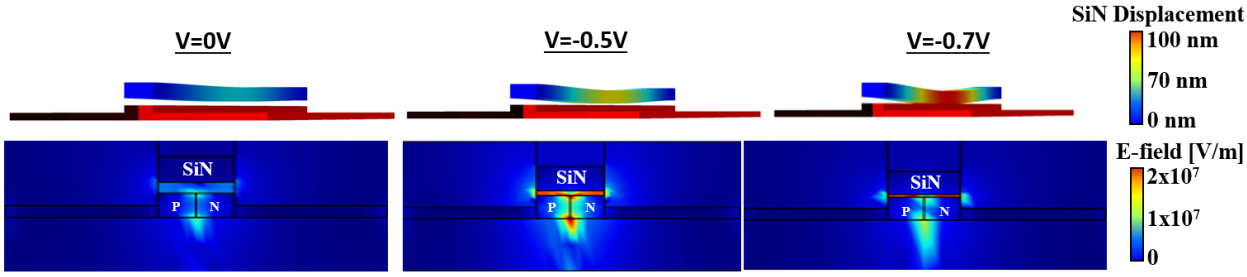

Figure 15: MEMS electromechanical simulation. (left to right) COMSOL electromechanical simulations showing beam deflections for 0V, 0.5V, 0.7V reverse bias. [bottom] (left to right) Corresponding electric field plots showing depletion region formation and E-field interaction with the SiN beam.

We constructed a 3D model of the proposed device in COMSOL using electromechanical multiphysics coupling between three physics interfaces – semiconductor, electrostatics, and solid mechanics. The silicon was doped with PPP/NNN and PP/NN in the slab regions, and P/N within the rib waveguide, creating a PN diode. This graded doping lowers the resistance from the waveguide to the highly doped terminals (which have a low ohmic contact resistance). As we increase the reverse biasing on the diode, the depletion region widens due to increased carrier re-combination, causing the electric field to increase in intensity both inside and outside the waveguide as seen in Fig. 15 [bottom]. This gradient in the electric field deflects the dielectric beam towards the center of the junction in the silicon waveguide. With a full actuation voltage of only V_{FA}=-0.7V (where the SiN meets the silicon – Fig. 15[top]), the effective index increases by Δn_{eff}=0.035 at the center of the beam. This index change results in a net phase shift of 1.41π with a 100 μm long SiN beam (Section 4.6, Fig. 25).

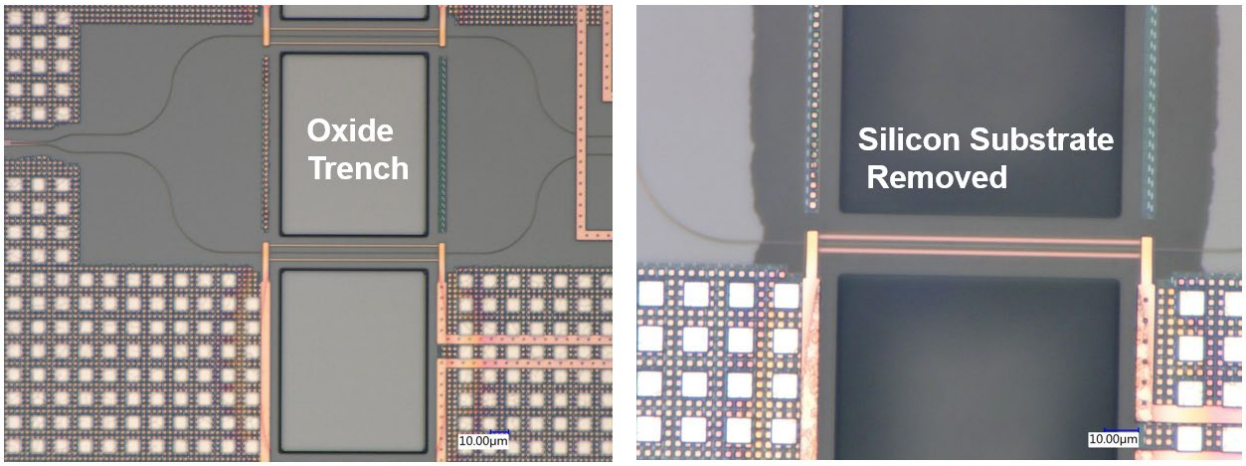

Figure 16: Thermally Isolated Phase Shifters. (left) Mach-Zehnder Interferometer with oxide trench. (right) Post-processing at RIT to etch away the silicon substrate underneath the heater/ phase-shifter.

The primary challenge with thermo-optic phase shifters is that they are inefficient. This results in high power usage, and as discussed earlier, significant crosstalk that makes it very challenging to realize complex PICs. However, the efficiency of thermal devices can be dramatically increased by selectively removing the silicon substrate under the heater, effectively eliminating the path of lowest thermal resistance, and thus isolating the device. Drawbacks of previous demonstrations of efficient undercut thermal phase shifters in the silicon-on-insulator (SOI) platform include the use of a backside etch for substrate removal [41] and fabrication in a low-volume e-beam platform [42]. In this project we realized a thermally isolated phase shifting cell fabricated by AIM Photonics, which exhibits low-crosstalk and low-power operation. MZI devices with thermal phase shifters were fabricated by AIM Photonics with a trench on either side of the waveguides terminating at the buried oxide layer (Figure 16). We post-processed at RIT by performing an Inductively Coupled Plasma (ICP) Reactive Ion Etching (RIE) etch of the remaining buried oxide to expose the silicon substrate. The silicon substrate was partially removed using a vapor phase xenon diflouride (XeF2) etch (resulting in 20μm undercut). As shown in Section 4.6, we achieved a Pπ, the power required for a phase shift of π, of 1.2 mW, which has a corresponding voltage of only Vπ=1.65 V. In addition, due to the dramatic performance increase of the air clad device we also found a significant improvement in thermal crosstalk.

3.4 Packaging

Robust packaging is critical for interfacing with and controlling quantum photonic chips, particularly as the circuit complexity increases. It also provides the thermal and mechanical stability needed for carrying out long term quantum experiments. Consequently, we have devoted significant efforts to developing integrated photonic packaging solutions that meet the demanding needs of quantum integrated photonics. Through our efforts we have realized complete packaging solutions that enable integrated photonic chips to be deployed into quantum experiment testbeds. In collaboration with AFRL, we packaged (Fig. 17) a quantum programmable processor (QPP) chip that implements an 8x8 programmable unitary circuit. The package has full electrical and optical connectivity to the chip, with a PCB that interfaces with the current quantum experimental testbed. The chip has 450 wire bonds, and it is a significant challenge to determine that all the connections are correctly made with no shorts/open circuits. To address this, we developed a packaging testbed (Figure 18) to automatically map the electrical paths. It achieves checks on 256 connections in less than 8 minutes (previously took more than an hour).

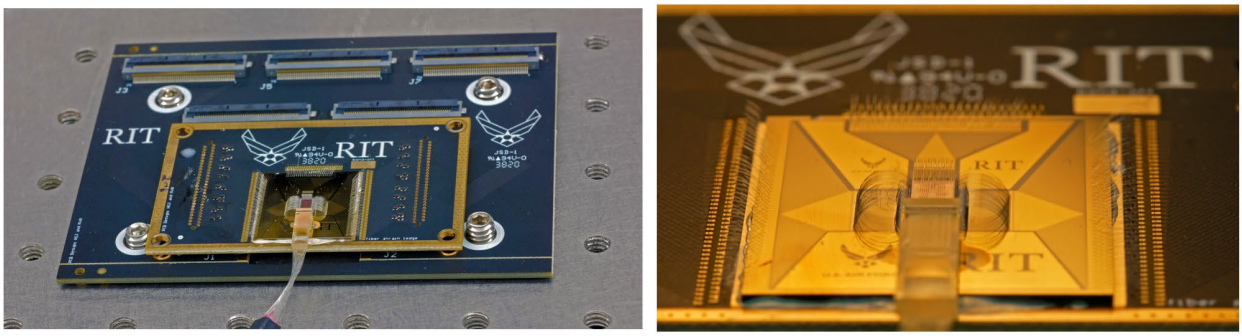

Figure 17: Packaged 8x8 Quantum Programmable Processor. RIT/AFRL Fully packaged 8x8 programmable unitary circuit (QPP) consisting of ~450 wire bonds with a 20-channel fiber array. The assembly is integrated into a testbed at RIT that is being transitioned to AFRL

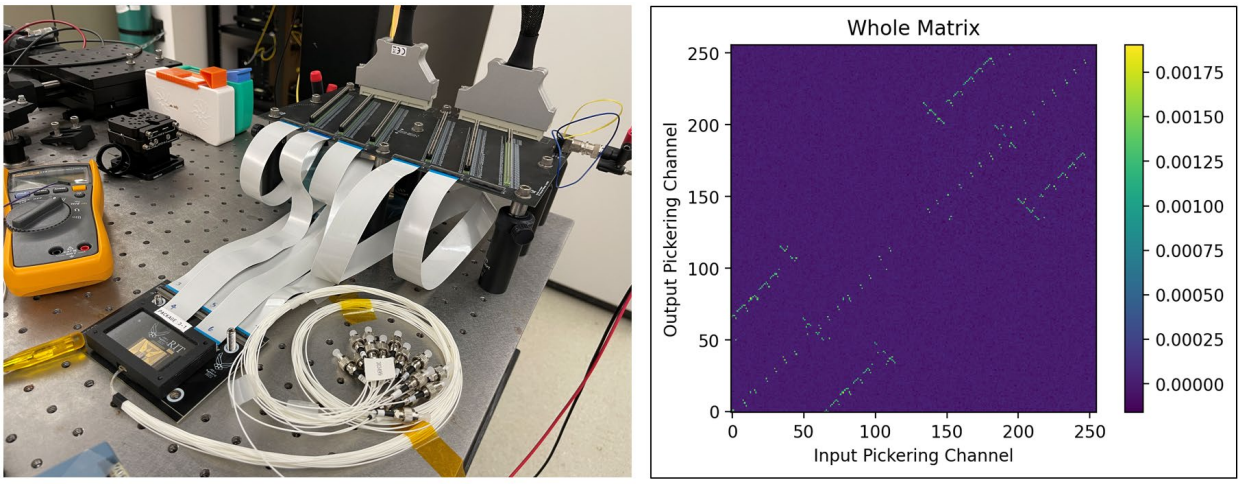

Figure 18: Packaging Testbed. Consists of Pickering 128x2 switch matrices, a custom PCB for interfacing with our packages using FFC (Flat-Flex-Cable) connectors. Python code checks every

connection possibility by switching every combination of connections and mapping the current, which is monitored using a Measurement Computing DAQ.

The most significant challenge with photonic chip packaging is the attachment of optical fibers. There are mechanical, thermal, and optical interfaces that must be optimized to demonstrate permanent attachment that achieves low loss. We have realized novel solutions, including, the use of high-NA optical fibers for ultra-low loss (<1.5dB) polarization independent coupling [43], and using the optimized edge couplers on the AFRL quantum wafers we have recently demonstrated low loss coupling (<1dB) directly to SMF28 (Fig. 19).

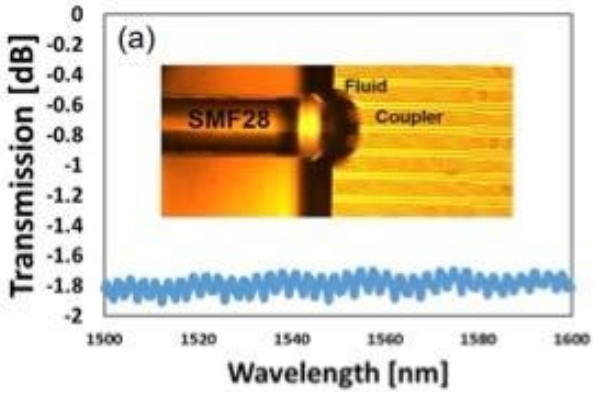

Figure 19: Ultra-low loss optical coupling and robust fiber attachment. Ultra-low loss coupling from SMF28 to a quantum PIC using an optimized coupler design. A coupling loss of <1dB/facet is achieved.

4.0 RESULTS AND DISCUSSION

4.1 Efficiently heralded silicon ring resonator photon-pair source

Presented here are results on a silicon ring resonator photon pair source with a high heralding efficiency [21]. As shown in Figure 3, previous ring resonator sources suffered from an effective 50% loss because to generate the photons the pump must be able to couple into the resonator which is an effective loss channel for the generated photon pairs. However, in practice the optical loss of the pump can be traded off for a dramatic increase in heralding efficiency (3.75× with a 10× increase in pump power). This was demonstrated experimentally by varying the separation (gap) between the input waveguide and the ring while maintaining a constant drop port gap (Figure 20). The ring resonator (R = 18.5μm, W = 500nm, and H = 220nm) was pumped by a tunable laser (λ~1550nm). The non-degenerate photons, produced via spontaneous four wave mixing, exited the ring resonator, and were coupled to fiber upon which they were filtered symmetrically about the pump. Coincidence counts were collected for all possible photon path combinations (thru and drop port) and the ratio of the drop port coincidences to the sum of the drop port and cross term coincidences (one photon from the drop port and one from the through port) was calculated.

With a 350nm pump waveguide gap (2.33× times larger than the drop port gap) we confirmed our theoretical predictions, with an observed improvement in heralding efficiency by a factor of ~ 2.61 (96.7% of correlated photons coupled out of the drop port). Furthermore, we verified that the experimental results match the theoretical predictions (Fig. 20) from Figure 3, by testing four

different ring resonator gaps. These results will enable increased photon flux integrated photon sources which can be utilized for high performance quantum computing and communication systems.

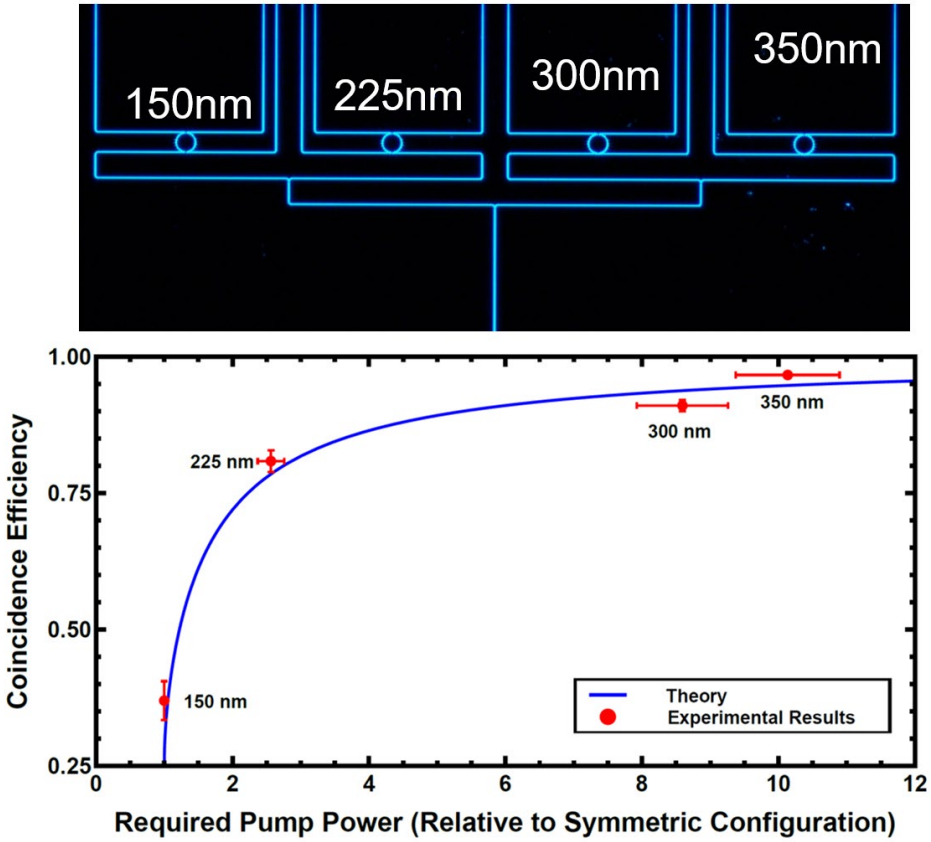

Figure 20: Experimental demonstration - tradeoff in source efficiency and pump power. (top) Microscope image of ring resonators with different gaps between the input waveguide and the microring resonator. (bottom) Experimental results and comparison to theory. The experimental results have an excellent agreement with the theory in Fig. 3. Specifically, the larger the input gap, the higher the required pump power but the coincidence efficiency increases to near unity.

4.2 Interferometrically coupled ring resonator photon source

Interferometric coupling overcomes the tradeoff, allowing simultaneous critical coupling of the pump laser into the ring resonator and high directivity of the photon pairs only to a single output port [22]. The net result is a photon source with the brightness of a critically coupled ring but with a coincidence/heralding efficiency of near unity. As shown in Figure 5, the device makes use of two MZI's which are designed to suppress alternating sets of resonances, with one set for pumping and the other for the photon pairs. The device was fabricated via the AIM Photonics foundry [Fig. 21(left)]. Thermal tuners were included with the device to allow for fine control of the optical path lengths of the ring and coupler arms. This allowed the device to operate as a lossy dual bus ring or in the desired highly directional configuration. The source was pumped with a tunable CW laser with 5dBm of optical power. Filters were placed before and after the photonic circuit to reduce noise and split the signal and idler photons. Coincident photon detections were integrated (with a 4-channel SNSPD and a TDC) for 300s with a timing resolution of 81 ps. The

results of these measurements are shown in Fig. 21. For the case of the lossy dual bus ring configuration, the coincidence efficiency was determined to be 78.5% while for the ideal optimized configuration, the coincidence efficiency was determined to be 99.8%. In addition, the coincidence rate increased from a peak of 26Hz by ten times to 260Hz, demonstrating that the pump laser is critically coupled which maximizes the generation of photon pairs. This work demonstrates that the coincidence efficiency of microring resonator sources can be increased to near unity by making use of multipoint interferometric couplers. In addition to the improved directionality, this configuration allows the pump to be critically coupled to the ring while the signal and idler photons can be overcoupled. This improved efficiency greatly increases the performance and scalability of integrated quantum information processing systems.

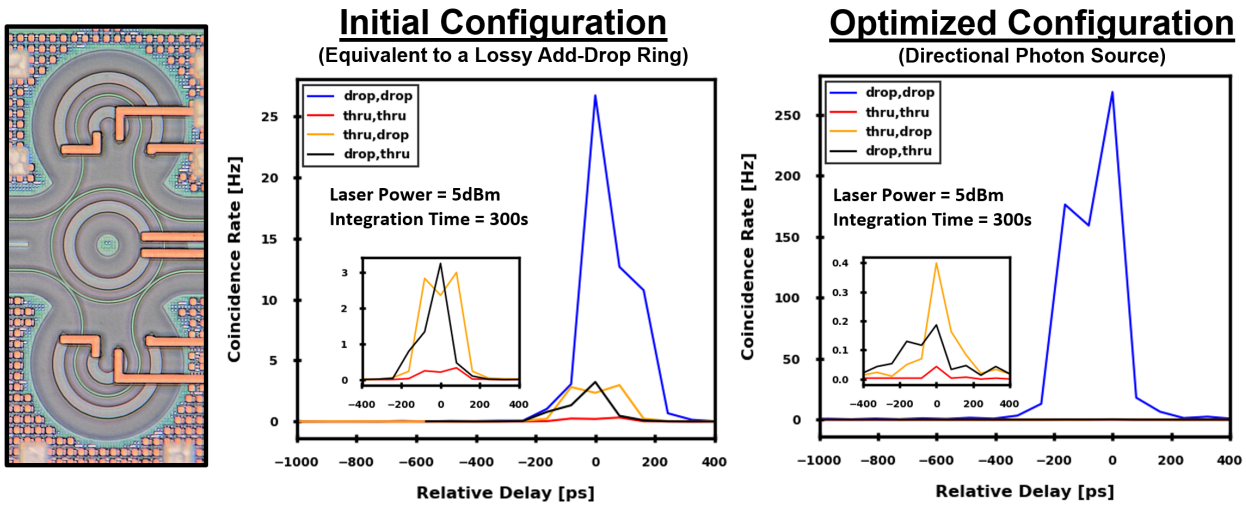

Figure 21: Interferometrically Coupled Microring Resonator Photon Source. (left) Microscope image of the source (Credit: M. Fanto, AFRL/RITQ). Coincident photon pair counts for the (middle) lossy dual bus ring configuration, and the (right) ideal directional source configuration.

4.3 TM-polarized photon source

Here we demonstrate a dual, nonlinearly coupled, resonator photon pair source for highly dispersive TM-polarized light [24,25]. By operating with TM polarization, it will be possible to realize improved filtering of the photon pairs. The two racetrack-style resonators are critically coupled to separate waveguides, as shown in Fig. 22(a). Each resonator can be independently tuned via resistive heating with voltages applied at V_1 and V_2. The two resonators interact via a directional coupler (DC) which is designed to ensure input light remains within resonator one. In this way, the two resonators are linearly uncoupled [26]. Pump light (green in the figure) was directed in through the input port, on resonance with resonator one. Due to the third order nonlinearity in silicon, signal, and idler photons in a wide range of wavelengths could be generated via SFWM in the first resonator. However, in the Directional Coupler (DC), signal and idler

photons that are resonant with resonator two are interferometrically enhanced, and couple into resonator two (blue/red in the figure). We note though that SFWM will only be enhanced when the resonances are equally spaced about the pump wavelength (Figure 6), a strict requirement for energy conservation. However, since the two resonators can be independently controlled, it is possible to realize efficient photon-pair generation (alignment of the resonances) even in the case where the individual resonators are highly dispersive.

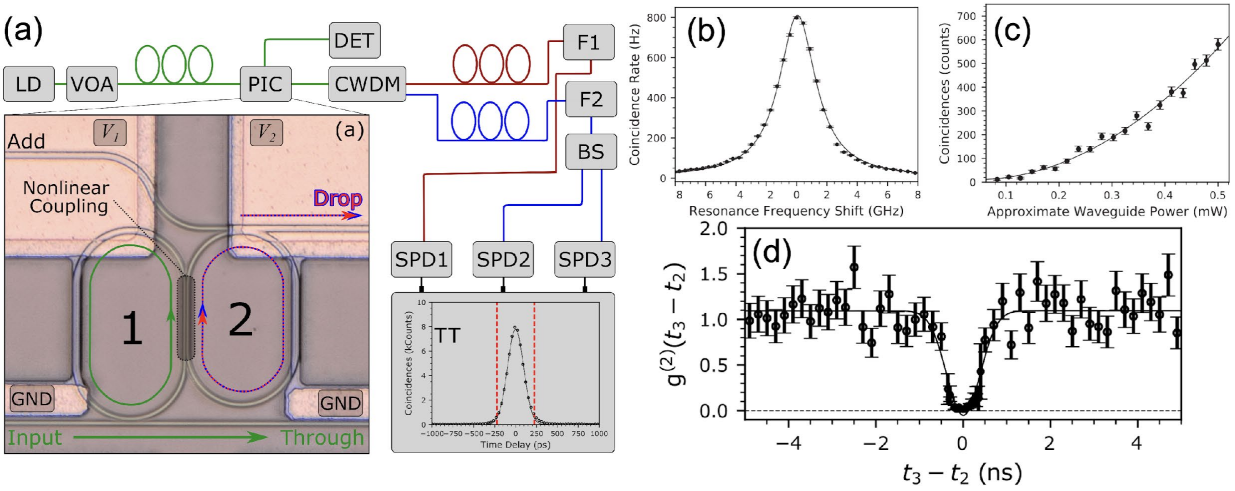

Figure 22: TM-polarized Photon Pair Source. (a) Light from a laser (LD) passes through a variable optical attenuator, polarization controller (PC) and then enters the photonic integrated circuit (PIC). Light is collected from the PIC and sent either to a detector (DET), or through a coarse wavelength division multiplexer (CWDM) to separate signal and idler photons. Each path then passes through polarization controllers and filters (F1 and F2). Signal photons are separated at a 50:50 beam splitter (BS) and then photons are detected via superconducting nanowire single photon detectors (SNSPDs) and correlated with a time tagger (TT). (a) PIC (fabricated using electron beam lithography with Applied Nanotools) showing the input pump field (green) and the signal and idler photons (blue and red) created in the DC and extracted through the drop port. Voltages $V_1$and V_2 are applied to tune the first and second resonators, respectively. The spectrum of the resonator is seen in Fig. 6(b). (b) Coincidences with the location of the resonances for resonator two are scanned via resistive heating. We include the Lorentzian least squares fit with a FWHM of 2.98 GHz. Each data point is collected with 3.0 minutes of integration. (c) The input pump power was varied, and coincidences were measured, exhibiting the quadratic behavior of the device. Error bars enclose one standard deviation. Input waveguide power was approximated based upon loss measurements. Values above 0.5 mW began to saturate the quadratic pair generation rate. (d) The value of $g^{(2)}$ as a function of the time delay between channels 2 and 3, where t_1=t_2=0. This data includes two sets of 10 hours of integration (with 200 ps and 50 ps bin sizes) and an average coincidence rate of 437 Hz. We show only the data for the smaller bin size near t_3−t_2=0 where triple coincidences are more common and error bars are small. A Gaussian fit to both sets of data combined gives a FWHM of 904 ps.

Figure 22(b) shows the efficient TM-polarized generation of photon pairs. To confirm that the dominant pair generation processes rely on the nonlinear coupling of the two resonators, we varied the heater current of resonator two to shift its resonances. The full width at half maximum

(FWHM) of a Lorentzian least squares fit was found to be 2.98 GHz, confirming that efficient photon-pair generation requires the resonances to be precisely aligned for energy conservation.

Since the SFWM process is nonlinear, we varied the input power to demonstrate the expected quadratic dependence as shown in Fig. 22(c). For each setting, the input power was set (with a maximum power of approximately 0.5mW) and the pump frequency and resonances of resonator two were scanned to optimize coincidence counts. Lastly, to analyze the quantum properties of the photon pairs, we performed a conditional second order self-correlation measurement ($g^{(2)}$) as shown in Fig. 22(d). With approximately 2.1mW of power in the input waveguide yielding 242 Hz coincidences, we measured a $g^{(2)}(0) = 0.044 \pm 0.004$, over 200 standard deviations below the classical threshold. Therefore, despite large group velocity dispersion we demonstrated phase matching in the SFWM process, made possible by the relatively short interaction length in the nonlinear coupling region and the interferometric enhancement of the second resonator. We obtained a maximum measured count rate of 2855 Hz with a CAR (Coincidental-to-Accidental Ratio) of 237 using 2.1 mW of pump power in the waveguide.

4.4 Two-photon interference in ring resonators on a photonic chip

Two-photon interference is the basis for realizing the manipulation of quantum states. We have achieved two-photon interference using a ring resonator for the first time. Specifically, previous demonstrations were done using directional couplers but that requires perfect control of the coupling (typically 50:50). In contrast, as shown in Figure 9 & 10, ring resonators offer a key advantage of a large parameter space where high performance two-photon interference can be achieved, in addition, within a highly compact device. Using the circuit in Figure 10 we measured two-photon and classical interference in Fig. 23 in a quantum ring resonator device. The classical interference realized 98% visibility [30]. Additionally, two-photon interference is also displayed (blue line) with the biphoton N00N (N=2) state exhibiting oscillations at twice the rate as the classical case. The raw visibility for the N00N state is as high as 95% demonstrating strong capability of achieving indistinguishable photons. The two-photon interference was adjusted by a rotation applied from the thermo-optic phase shifters preceding the quantum ring resonators. These rotations are implemented by biasing heaters in the coupled rings and establishing a relative phase shift. When the potential difference between the upper and lower ring heaters is set to 7V, a$\sim\pi$ rotation is induced making the coupled ring system act as a tunable beam splitter.

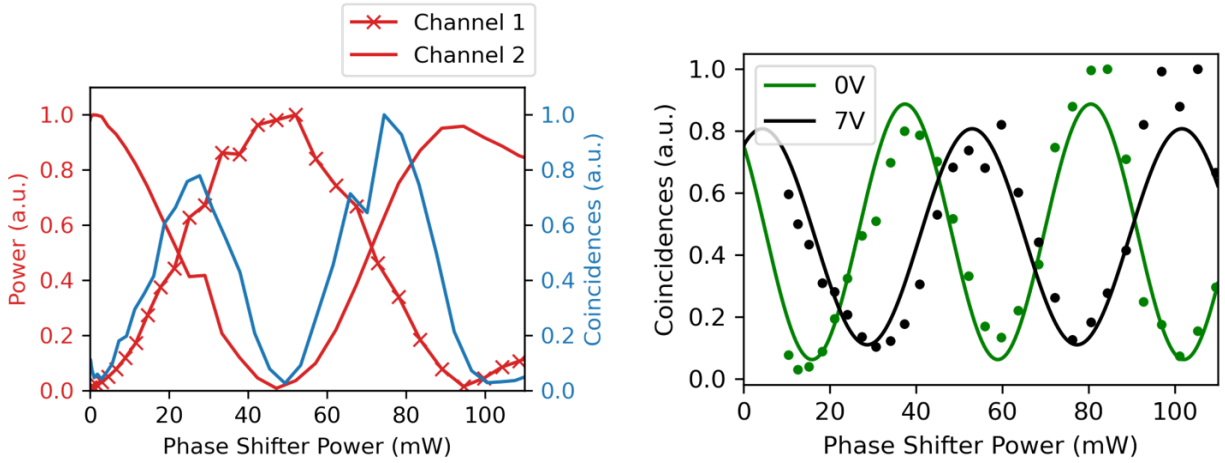

Figure 23: Two-photon interference in a quantum ring resonator. (left) Interference fringes as a function of the phase shifter voltage preceding the quantum ring resonator for both the classical case (red lines) and quantum biphotons (blue line). The biphotons oscillate at twice the rate, as predicted by quantum theory for a two-photon N00N state. (right) The coupled ring resonator heaters are biased to induce a relative phase shift in the interference pattern (no phase change = green; π phase shift = black).

4.5 Two-photon interference from independent resonant sources

Linear optical quantum computing relies on the ability to manipulate single-photons through high-visibility interference effects. This requires the generation of indistinguishable photons from independent photon sources. Figure 11 shows a PIC circuit which consists of two interferometrically coupled microring resonator photon sources. A key advantage of these sources is that the bandwidth of the resonator can be tuned, enabling the generated biphoton bandwidths to be matched (along with their central frequency). Following the two sources the circuit continues to thermo-optic phase shifters and a Mach-Zehnder Interferometer, which is used to determine the biphoton pairs indistinguishability through two-photon interference.

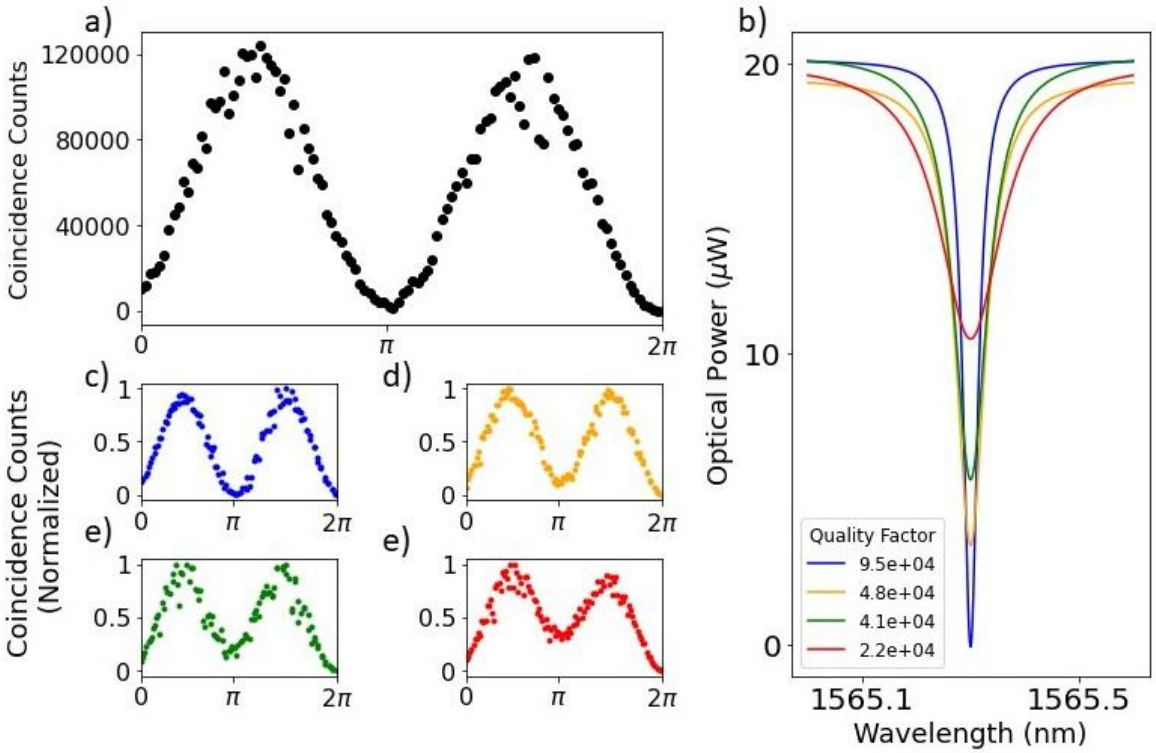

Figure 24: Two-photon interference from independent resonant sources. (a) Interference pattern for two interferometrically coupled microring photon sources when the pumps are critically coupled. (b) Source 1's pump ring resonator spectra is tuned from critical (blue) to over-coupled (red). The spectra are fitted to a Lorentzian (not shown). The second source is fixed at critical coupling. (c-f) Corresponding two-photon interference patterns. The coincidence counts in all figures are calculated by subtracting accidentals taken from far outside the coincidence window.

The two-photon interference measurements are presented in Figure 24. We measured a maximum coincidence counting rate of 3.3 kHz with both sources configured to have critically coupled pumps. In order to determine the impact of the resonator bandwidth on visibility, the pump coupling of Source #1 was varied from critical coupled to over-coupled (Fig. 24 (b)). The corresponding interference patterns are shown in Figure 24(c-f), which achieved visibilities of 99.2% [Q=9.5e+4], 81.8% [Q=4.8e+4], 73.7% [Q=4.1e+4], and 55.5% [Q=2.2e+4]. In addition to the resonator's bandwidth, the change in the directivity (Section 4.2) of the photon source will influence the flux of photon pairs exiting from Source #1. The relationship between these two effects is continuing to be investigated.

4.6 Micro-electro-mechanical (MEMs) Phase Shifters

MEMs phase shifters are a promising approach for realizing phase shifting with low loss, low energy use and minimal crosstalk. In this project we showed (Figure 14 & 15) a foundry compatible design [12] that with a full actuation voltage of only V_{FA}=-0.7V (where the SiN comes into contact with the silicon – Figure 17[top]), yields a net phase shift of 1.41π with a 100 μm long SiN beam (Fig. 25[left]). We also explored the phase change for a SiN beam that is 10nm thicker [230nm total], which yielded an even larger phase shift of 1.83π with V_{FA} = -0.9V. We also

investigated the dependence on the initial gap between the SiN beam and silicon and found that even with a 200nm gap the device has a low V_{FA}=-5V (1.85π) and a 300nm gap requires V_{FA}=-12V (1.53π).

Using Lumerical 3D FDTD simulations, we determined that the phase shifter's total insertion loss is very low (<0.5dB). Specifically, because most of the optical mode is confined within the silicon rib waveguide, the transition from oxide to the air trench (with the SiN beam 100nm above the silicon waveguide) has a scattering loss of less than -0.017dB. Furthermore, because the effective index change along the beam is very gradual, the mode is adiabatically transformed along the length of the beam, with no additional loss. The only appreciable loss is due to the PN doping, which is estimated to only be 0.2-0.3dB over the entire length of the device (20-30dB/cm with P/N doping) and can be further optimized.

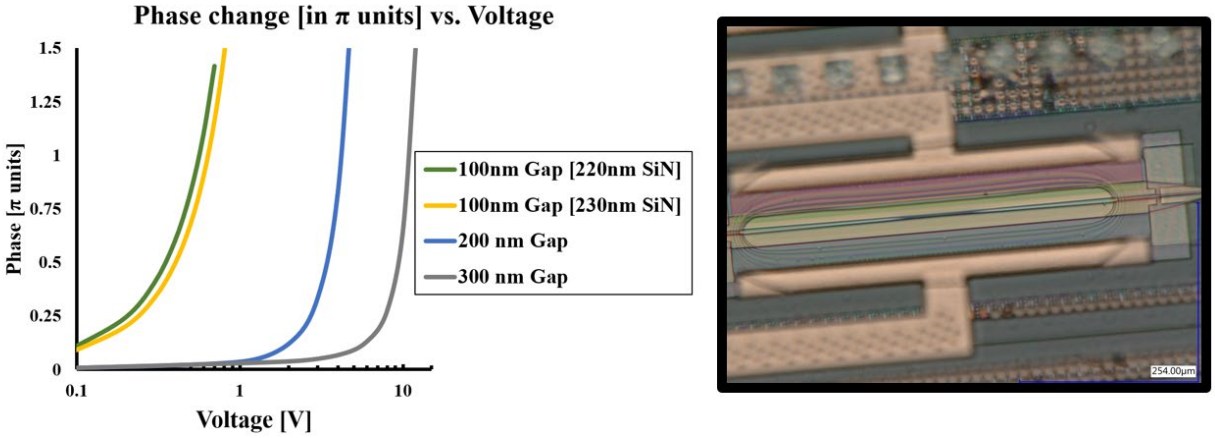

Figure 25: MEMs phase shifter. [left] Phase (in π units) vs. Voltage - for 100µm long SiN beam with varying gaps: 100 nm (220 nm & 230 nm thick SiN), and 200 nm and 300 nm gaps (with 220nm thick SiN). **[right]** Microscope image of a post-processed MEMs phase shifter with a release SiN beam.

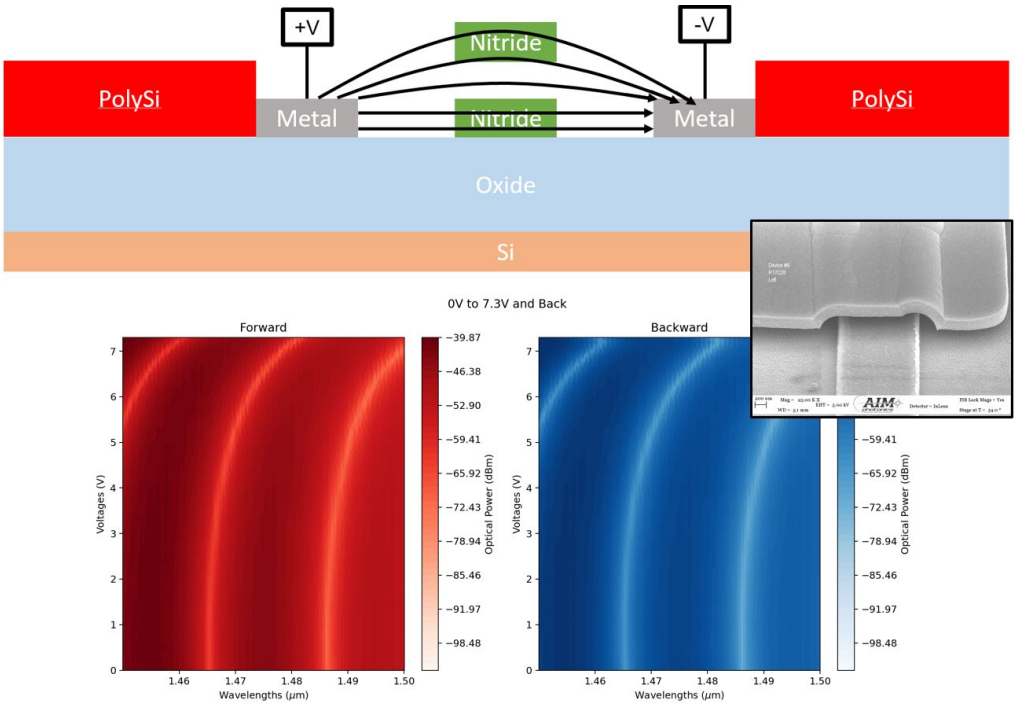

Figure 26: Low voltage SiN MEMs Phase Shifter. [top] Cross-section of the SiN MEMS device qualitatively demonstrating the operation of the device where voltage is applied to metal electrodes, creates a gradient electric field that actuates a nitride beam. The nitride beam is released by etching Polysilicon using a vapor XeF2 etch, enabling wafer scale release. **[bottom]** Inset: Scanning electron microscope (SEM) image of the Nitride single-sided beam anchor (wide and short single-clamped cantilever) released above a SiN waveguide. The transmission of a MZI with the phase shifter realizes a π phase shift with 7V, and it is highly repeatable (forward/backward operation is very similar).

We recently demonstrated a preliminary version of the design without dopants, and larger electrode separation [12]. In addition, as shown in Fig. 25 [right] we have successfully post processed the complete design and released the SiN beam using a standard wet hydrofluoric acid etch with critical point drying. We are now working to integrate the complete fabrication and release process fully in the foundry.

Previous works have demonstrated silicon nitride MEMs phase tuning through vertically displaced microbridges [35]. However, these have required >40 V for a π phase shift. Ultra-low voltage (~1 V) designs using horizontal slot waveguides have recently been demonstrated [45,46] although these methods require complex mechanical structures that must be released using vapor-HF or critical point drying post-processing. We have recently demonstrated low-voltage phase tuning of vertically actuated beams that are released at wafer level with a vapor XeF2 etch completely in-house [47]. Our process is carried out on an i-line photolithography stepper to define the waveguiding, metal, and MEMS structures. We use a sacrificial polysilicon layer between the SiN waveguide and the SiN beam (Figure 26). The XeF2 undercuts the beam, enabling a simple MEMs release process that does not undercut the waveguide. The movable SiN beam on top of the waveguide utilizes a single-sided anchor so that it resembles a wide and short single-clamped cantilever. This enables a phase shifter that is capable of a π phase shift with <10 V and length <100μm. We measured the optical transmission versus applied voltage for multiple voltage

sweeps and extract the phase shift per voltage at various wavelengths (Fig. 26). We demonstrate reliable tuning over multiple sweeps with an average voltage of 7V±0.5V for a π phase shift. This phase shifter is central to the scalability of programmable quantum photonic circuits.

4.7 Isolated thermo-optic phase shifter

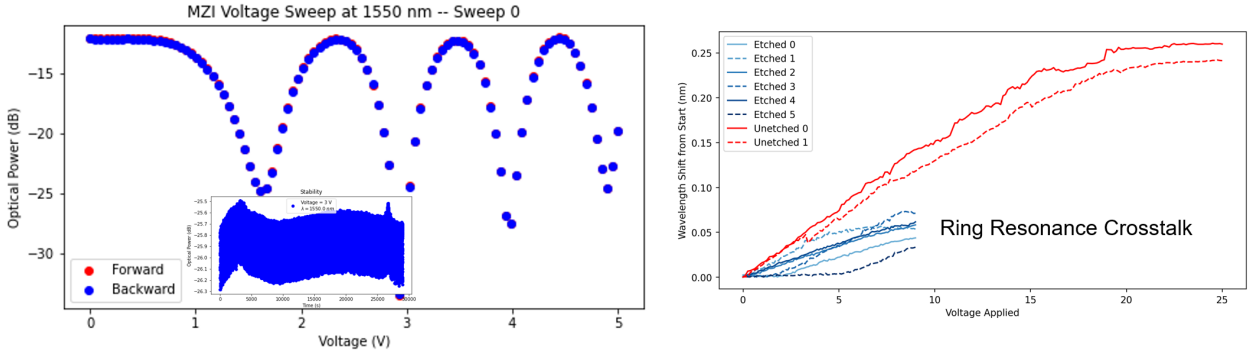

Figure 27: Thermally isolated thermo-optic phase shifter. [left] Optical power of an MZI as the thermally isolated phase shifter volage is applied. π is achieved with only 1.2mW (1.75V), and more than 7π is achieved in under 5V. The inset shows the heater is highly stable when applied to 3π. **[right]** Demonstration of thermal crosstalk of this standard (unetched) and air clad (etched) devices, as measured by tracking the resonance shift of a nearby microring resonator. The scans were repeated multiple times.

We present a thermally isolated phase shifter realized by undercutting the silicon waveguide and integrated doped-Silicon resistive heater (Fig. 16). By removing the Silicon substrate, the generated heat is isolated by the surrounding air, dramatically improving efficiency. Specifically, the standard thermo-optic heater requires tens of milliwatts to realize a π phase shift. As seen in Figure 27, the isolated phase shifter achieves a π shift with only 1.2mW (1.75V). Furthermore, the phase shifter is highly stable as shown in the inset.

We determine the isolation of the thermal phase shifter by tracking the resonance peak wavelength of a nearby (~500μm) ring resonator – a highly temperature sensitive device. We applied an increasing range of voltages to the thermal phase shifter, while optically probing the ring resonator. We investigate the resonance shift as a function of heat in the thermal phase shifter, shown in Fig. 16 (right). The standard device (unetched) shifts the resonance more than the air clad (etched) for the same power, demonstrating the thermal isolation of the heaters. In addition, due to the dramatic performance increase of the air clad device we also note the difference in resonance shift at the operating power. The standard device has a characterized Pπ= 60 mW (~12V) and induces a 170 pm resonance shift at that power, whereas the air clad thermally isolated device has Pπ= 1.2 mW, inducing a resonance shift of only 20 pm at that operating point. Consequently, an effective order of magnitude reduction in crosstalk will be realized in practice.

5.0 CONCLUSIONS

We have developed, in collaboration with AFRL/RITQ and AIM Photonics, a 300mm photonic wafer platform that is optimized for quantum photonics with low loss Silicon & Silicon Nitride waveguides, and edge couplers with <1dB coupling to optical fibers. In addition, it has passive & active elements for realizing high performance electro-optic modulation, efficient thermo-optic phase shifters, MEMs, and the hybrid integration of quantum materials/devices (single photon emitters and detectors). We have developed all the key building blocks, including, high performance photon sources, phase shifters for controlling the quantum state and circuits for interfering the photons and controlling entanglement.

In this project a key focus was on the realization of high-performance resonant photon sources. We identified a key tradeoff in source brightness and efficiency [21], and overcame the tradeoff [20,22] with a novel integration of interferometric coupling into the microring resonator to realize a photon source that has near-unity heralding efficiency and high brightness. We also demonstrated quantum interference with the photon source in novel circuit configurations [30,31]. We identified thermal crosstalk as a significant obstacle towards realizing complex quantum circuits, and investigated alternatives based on MEMs [12,40,47]. We also optimized the performance of the thermo-optic phase shifter to realize ~1mW operation with minimal crosstalk.

We have also developed novel packaging solutions, further improving fiber coupling efficiency and reliability [44], and electrical interconnect density. Testbeds for characterizing the packages were created to carry out quantum experiments (discrete, microcontroller and FPGA based, hardware/software interfaces to test equipment, data acquisition boards and software algorithms). Overall, this work has established the foundation for all the components and packaging technologies needed for scaling up to large-scale quantum information processing with hundreds or even thousands of photons.

6.0 REFERENCES

1. J. Wang, F. Sciarrino, A. Laing, and M. G. Thompson, "Integrated photonic quantum technologies," Nat. Photonics **14**, 273–284 (2020).
2. J. M. Arrazola, V. Bergholm, K. Brádler, T. R. Bromley, M. J. Collins, I. Dhand, A. Fumagalli, T. Gerrits, A. Goussev, L. G. Helt, J. Hundal, T. Isacsson, R. B. Israel, J. Izaac, S. Jahangiri, R. Janik, N. Killoran, S. P. Kumar, J. Lavoie, A. E. Lita, D. H. Mahler, M. Menotti, B. Morrison, S. W. Nam, L. Neuhaus, H. Y. Qi, N. Quesada, A. Repingon, K. K. Sabapathy, M. Schuld, D. Su, J. Swinarton, A. Száva, K. Tan, P. Tan, V. D. Vaidya, Z. Vernon, Z. Zabaneh, and Y. Zhang, "Quantum circuits with many photons on a programmable nanophotonic chip," Nature **591**, 54–60 (2021).
3. D. Bunandar, A. Lentine, C. Lee, H. Cai, C. M. Long, N. Boynton, N. Martinez, C. Derose, C. Chen, M. Grein, D. Trotter, A. Starbuck, A. Pomerene, S. Hamilton, F. N. C. Wong, R. Camacho, P. Davids, J. Urayama, and D. Englund, "Metropolitan Quantum Key Distribution with Silicon Photonics," Phys. Rev. X **8**, 021009 (2018).
4. N. H. Wan, T. J. Lu, K. C. Chen, M. P. Walsh, M. E. Trusheim, L. De Santis, E. A. Bersin, I. B. Harris, S. L. Mouradian, I. R. Christen, E. S. Bielejec, and D. Englund, "Large-scale integration of artificial atoms in hybrid photonic circuits," Nature **583**, 226–231 (2020).
5. J. Zhao, C. Ma, M. Rüsing, and S. Mookherjea, "High Quality Entangled Photon Pair Generation in Periodically Poled Thin-Film Lithium Niobate Waveguides," Phys. Rev. Lett. **124**, 163603 (2020).
6. F. Najafi, J. Mower, N. C. Harris, F. Bellei, A. Dane, C. Lee, X. Hu, P. Kharel, F. Marsili, S. Assefa, K. K. Berggren, and D. Englund, "On-chip detection of non-classical light by scalable integration of single-photon detectors.," Nat. Commun. **6**, 5873 (2015).
7. F. Lecocq, F. Quinlan, K. Cicak, J. Aumentado, S. A. Diddams, and J. D. Teufel, "Control and readout of a superconducting qubit using a photonic link," Nature **591**, 575–579 (2021).
8. R. J. Niffenegger, J. Stuart, C. Sorace-Agaskar, D. Kharas, S. Bramhavar, C. D. Bruzewicz, W. Loh, R. T. Maxson, R. McConnell, D. Reens, G. N. West, J. M. Sage, and J. Chiaverini, "Integrated multi-wavelength control of an ion qubit," Nature **586**, 538–542 (2020).

9. L. Carpenter, M. van Niekerk, A. Begovic, V. Sundaram, V. Deenadayalan, T. Palone, M. Fanto, S. Preble, C. Baiocco, G. Leake, N. Fahrenkopf, and D. Harame, "Towards Low Propagation Losses in Active Photonic Multi-Project Wafer Runs," in *OSA Advanced Photonics Congress* (2021).
10. V. Deenadayalan, M. van Niekerk, M. Fanto, and S. Preble, "Silicon Photonic MEMS Phase Shifter Using Gradient Electric Force Actuation," in *Frontiers in Optics / Laser Science (2020), Paper FW5D.3* (The Optical Society, 2021), p. FW5D.3.
11. N. Lindenmann, G. Balthasar, D. Hillerkuss, R. Schmogrow, M. Jordan, J. Leuthold, W. Freude, and C. Koos, "Photonic wire bonding: a novel concept for chip-scale interconnects," Opt. Express **20**, 17667 (2012).
12. M. W. Pruessner, D. A. Kozak, N. A. Tyndall, W. S. Rabinovich, V. Deenadayalan, M. Fanto, S. Preble, and T. H. Stievater, "Foundry-processed optomechanical photonic integrated circuits," OSA Contin. **4**, 1215–1222 (2021).
13. C. Kieninger, Y. Kutuvantavida, D. L. Elder, S. Wolf, H. Zwickel, M. Blaicher, J. N. Kemal, M. Lauermann, S. Randel, W. Freude, L. R. Dalton, and C. Koos, "Ultra-high electro-optic activity demonstrated in a silicon-organic hybrid modulator," Optica **5**, 739–748 (2018).
14. S. F. Preble, M. L. Fanto, J. A. Steidle, C. C. Tison, G. A. Howland, Z. Wang, and P. M. Alsing, "On-Chip Quantum Interference from a Single Silicon Ring-Resonator Source," Phys. Rev. Appl. **4**, 021001 (2015).
15. Z. Vernon, M. Menotti, C. C. Tison, J. A. Steidle, M. L. Fanto, P. M. Thomas, S. F. Preble, A. M. Smith, P. M. Alsing, M. Liscidini, and J. E. Sipe, "Truly unentangled photon pairs without spectral filtering," Opt. Lett. **42**, (2017).
16. C. Ma, X. Wang, and S. Mookherjea, "Progress towards a widely usable integrated silicon photonic photon-pair source," OSA Contin. **3**, 1398 (2020).
17. C. Ma and S. Mookherjea, "Prospects for photon-pair generation using silicon microring resonators with two-photon absorption and free carrier absorption," OSA Contin. **3**, 1138 (2020).
18. M. L. Fanto, A. M. Smith, P. M. Alsing, C. C. Tison, S. F. Preble, G. E. Lott, J. M. Osman, A. Szep, and R. S. Kim, "A periodic probabilistic photonic cluster state generator," in *SPIE Security + Defence*, M. T. Gruneisen, M. Dusek, J. G. Rarity, K. L. Lewis, R. C. Hollins, T. J. Merlet, and A. Toet, eds. (International Society for Optics and Photonics, 2014), p. 92540J.

19. I. I. Faruque, G. F. Sinclair, D. Bonneau, J. G. Rarity, and M. G. Thompson, "On-chip quantum interference with heralded photons from two independent micro-ring resonator sources in silicon photonics," arXiv **26**, 20379–20395 (2017).
20. C. C. Tison, J. A. Steidle, M. L. Fanto, Z. Wang, N. A. Mogent, A. Rizzo, S. F. Preble, and P. M. Alsing, "Path to increasing the coincidence efficiency of integrated resonant photon sources," Opt. Express **25**, (2017).
21. J. A. Steidle, M. L. Fanto, C. C. Tison, Z. Wang, P. M. Alsing, and S. F. Preble, "Efficiently heralded silicon ring resonator photon-pair source," in E. Donkor and M. Hayduk, eds. (International Society for Optics and Photonics, 2016), p. 987304.
22. J. A. Steidle, C. C. Tison, M. L. Fanto, S. F. Preble, and P. M. Alsing, "Highly Directional Silicon Microring Photon Pair Source," in *Conference on Lasers and Electro-Optics (2019), Paper FTh1D.4* (The Optical Society, 2019), p. FTh1D.4.
23. Z. Vernon, M. Liscidini, and J. E. Sipe, "No free lunch: the trade-off between heralding rate and efficiency in microresonator-based heralded single photon sources," Opt. Lett. Vol 41 Issue 4 Pp 788-791 **41**, 788–791 (2016).
24. D. J. Starling, J. Poirier, M. Fanto, J. A. Steidle, C. C. Tison, G. A. Howland, and S. F. Preble, "TM Polarized Photon Pair Generation in Linearly Uncoupled Silicon Resonators," in *CLEO: QELS_Fundamental Science* (Optical Society of America, 2020), p. FTu4C—-2.
25. D. J. Starling, J. Poirier, M. Fanto, J. A. Steidle, C. C. Tison, G. A. Howland, and S. F. Preble, "Nonlinear Photon Pair Generation in a Highly Dispersive Medium," Phys. Rev. Appl. **13**, 041005 (2020).
26. M. Menotti, B. Morrison, K. Tan, Z. Vernon, J. E. Sipe, and M. Liscidini, "Nonlinear Coupling of Linearly Uncoupled Resonators," Phys. Rev. Lett. **122**, 013904 (2019).
27. C. K. Hong, Z. Y. Ou, and L. Mandel, "Measurement of subpicosecond time intervals between two-photons by interference," Phys. Rev. Lett. **59**, 2044–2046 (1987).
28. E. Knill, R. Laflamme, and G. J. Milburn, "A scheme for efficient quantum computation with linear optics.," Nature **409**, 46–52 (2001).
29. E. E. Hach, S. F. Preble, A.W. Elshaari, P. M. Alsing, and M. L. Fanto, "Scalable Hong-Ou-Mandel manifolds in quantum-optical ring resonators," Phys. Rev. - At. Mol. Opt. Phys. **89**, (2014).

30. J. Serafini, D. Spiecker, J. Steidle, M. Fanto, E. Hach, and S. Preble, "Two-photon interference via coupled ring resonators on a silicon photonic chip," in *CLEO: QELS_Fundamental Science* (Optical Society of America, 2020), p. FTu4C—-7.
31. J. Serafini, M. van Niekerk, M. Fanto, and S. Preble, "Tunable, High Purity Two-Photon Interference From Independent Sources On a Silicon Photonic Chip," in *2021 IEEE Photonics Conference (IPC)* (2021), pp. 1–2.
32. Y. Liu, C. Wu, X. Gu, Y. Kong, X. Yu, R. Ge, X. Cai, X. Qiang, J. Wu, X. Yang, and P. Xu, "High-spectral-purity photon generation from a dual-interferometer-coupled silicon microring," Opt. Lett. **45**, 73 (2020).
33. H.-S. Zhong, H. Wang, Y.-H. Deng, M.-C. Chen, L.-C. Peng, Y.-H. Luo, J. Qin, D. Wu, X. Ding, Y. Hu, P. Hu, X.-Y. Yang, W.-J. Zhang, H. Li, Y. Li, X. Jiang, L. Gan, G. Yang, L. You, Z. Wang, L. Li, N.-L. Liu, C.-Y. Lu, and J.-W. Pan, "Quantum computational advantage using photons," Science **370**, 1460–1463 (2020).
34. W. R. Clements, P. C. Humphreys, B. J. Metcalf, W. S. Kolthammer, and I. A. Walmsley, "Optimal design for universal multiport interferometers," Optica **3**, 1460–1465 (2016).
35. M. W. Pruessner, D. Park, B. J. Roxworthy, D. A. Kozak, T. H. Stievater, N. F. Tyndall, and W. S. Rabinovich, "Loss reduction in electromechanically tunable microring cavities," Opt. Lett. **44**, 3346 (2019).
36. S. Han, T. J. Seok, N. Quack, B.-W. Yoo, and M. C. Wu, "Large-scale silicon photonic switches with movable directional couplers," Optica **2**, 370 (2015).
37. C. Bekker, C. G. Baker, R. Kalra, H. H. Cheng, B. B. Li, V. Prakash, and W. P. Bowen, "Free spectral range electrical tuning of a high quality on-chip microcavity," arXiv **26**, 33649–33670 (2018).
38. V. Deenadayalan, M. van Niekerk, M. Fanto, and S. Preble, "Silicon Photonic MEMS Phase Shifter Using Gradient Electric Force Actuation," in *Frontiers in Optics* (2020), pp. FW5D--3.
39. V. Deenadayalan, M. Fanto, M. Van Niekerk, and S. Preble, "Ultra-Low Voltage Silicon Photonic MEMS Phase Shifter," in *2020 IEEE Photonics Conference, IPC 2020 - Proceedings* (Institute of Electrical and Electronics Engineers Inc., 2020).

40. V. Deenadayalan, M. Fanto, M. Van Niekerk, and S. Preble, "Ultra-Low Voltage Silicon Photonic MEMS Phase Shifter," in *2020 IEEE Photonics Conference, IPC 2020 - Proceedings* (Institute of Electrical and Electronics Engineers Inc., 2020).
41. J. E. Cunningham, I. Shubin, X. Zheng, T. Pinguet, A. Mekis, Y. Luo, H. Thacker, G. Li, J. Yao, K. Raj, and A. V. Krishnamoorthy, "Highly-efficient thermally-tuned resonant optical filters," Opt. Express **18**, 19055–19063 (2010).
42. P. Sun and R. M. Reano, "Submilliwatt thermo-optic switches using free-standing silicon-on-insulator strip waveguides," Opt. Express **18**, 8406–8411 (2010).
43. P. Yin, J. R. Serafini, Z. Su, R.-J. Shiue, E. Timurdogan, M. L. Fanto, and S. Preble, "Low connector-to-connector loss through silicon photonic chips using ultra-low loss splicing of SMF-28 to high numerical aperture fibers," Opt. Express **27**, (2019).
44. G. Bond, T. Palone, M. Van Niekerk, J. Serafini, M. J. Ciminelli, M. L. Fanto, and S. F. Preble, "Direct attachment of optical fibers to photonic integrated circuits with in situ UV curing," in *Conference on Lasers and Electro-Optics (CLEO)* (2021).
45. T. Grottke, W. Hartmann, C. Schuck, and W. H. P. Pernice, "Optoelectromechanical phase shifter with low insertion loss and a pi tuning range," Opt. Express **29**, 5525–5537 (2021).
46. R. Baghdadi, M. Gould, S. Gupta, M. Tymchenko, D. Bunandar, C. Ramey, and N. C. Harris, "Dual slot-mode NOEM phase shifter," Opt. Express **29**, 19113–19119 (2021).
47. McNulty, Karl, M. Van Niekerk, V. Deenadayalan, Errando-Herranz, Carlos, M. W. Pruessner, M. L. Fanto, and Preble, Stefan F., "Wafer Scale Fabrication of Silicon Nitride MEMS Phase Shifters With XeF2Dry Vapor Release Etch Process," in *SPIE OPTO: Silicon Photonics XVII* (2022), pp. 12006–32.
48. T. Barwicz, Y. Taira, T. W. Lichoulas, N. Boyer, Y. Martin, H. Numata, J.-W. Nah, S. Takenobu, A. Janta-Polczynski, E. L. Kimbrell, R. Leidy, M. H. Khater, S. Kamlapurkar, S. Engelmann, Y. A. Vlasov, and P. Fortier, "A Novel Approach to Photonic Packaging Leveraging Existing High-Throughput Microelectronic Facilities," IEEE J. Sel. Top. Quantum Electron. **22**, 455–466 (2016).
49. J. Nauriyal, M. Song, R. Yu, and J. Cardenas, "Fiber-to-chip fusion splicing for low-loss photonic packaging," Optica **6**, 549–552 (2019).

50. S. Khan, S. M. Buckley, J. Chiles, R. P. Mirin, S. W. Nam, and J. M. Shainline, "Low-loss, high-bandwidth fiber-to-chip coupling using capped adiabatic tapered fibers," APL Photonics **5**, 056101 (2020).

APPENDIX A – PUBLICATIONS AND PRESENTATIONS

Journal

1. Marcel W. Pruessner, Dmitry A. Kozak, Nathan A. Tyndall, William S. Rabinovich, Venkatesh Deenadayalan, Michael Fanto, Stefan Preble, and Todd H. Stievater, "Foundry-processed optomechanical photonic integrated circuits," OSA Continuum 4, 1215-1222 (2021).
2. Matthew van Niekerk, Saman Jahani, Justin Bickford, Pak Cho, Stephen Anderson, Gerald Leake, Daniel Coleman, Michael L. Fanto, Christopher C. Tison, Gregory A. Howland, Zubin Jacob, Stefan F. Preble, "Two-dimensional extreme skin depth engineering for CMOS photonics," J. Opt. Soc. Am. B 38, 1307-1316 (2021).
3. David J. Starling, Jacob Poirier, Michael Fanto, Jeffrey A. Steidle, Christopher C. Tison, Gregory A. Howland, Stefan F. Preble, "Nonlinear Photon Pair Generation in a Highly Dispersive Medium," Physical Review Applied 13, 041005 (2020).
4. T.-Ju Lu, M. L. Fanto, H. Choi, P. Thomas, J. Steidle, S. Mouradian ,W. Kong, D. Zhu, H. Moon, K. Berggren, J. Kim, M. Soltani, S. F. Preble, D. Englund, "An Aluminum Nitride Integrated Photonics Platform for the Ultraviolet to Visible Spectrum," Optics Express 26, 11147 (2018).
5. C. C. Tison, J.A. Steidle, M. L. Fanto, Z. Wang, N. A. Mogent, A. Rizzo, S. F. Preble, P. M. Alsing, "The path to increasing the heralding efficiency of integrated photon sources," Optics Express 25, 33088 (2017).
6. Z. Vernon, M. Menotti, C. C. Tison, J.A. Steidle, M. L. Fanto, P. M. Thomas, S. F. Preble, A. M. Smith, P. M. Alsing, M. Liscidini, J.E. Sipe, "Truly unentangled photon pairs without spectral filtering," Optics Letters 42, 3638 (2017).
7. J.A. Steidle, M.L. Fanto, C.C. Tison, G.A. Howland, E.E. Hach III, Z. Wang, P.M. Alsing, S. F. Preble, "Measurement of Quantum Interference in a Silicon Ring-Resonator Photon Source," Journal of Visualized Experiments 122, e55257 (2017).

Conferences / Workshops

1. Karl McNulty, Matthew van Niekerk, Venkatesh Deenadayalan, Carlos Errando-Herranz, Marcel Pruessner, Michael L. Fanto, and Stefan F. Preble, "Wafer Scale Fabrication of Silicon Nitride MEMS Phase Shifters With XeF2Dry Vapor Release Etch Process," SPIE Photonics West 2022, SPIE OPTO, Silicon Photonics XVII, 12006-32, January 2022.
2. John Serafini, Matthew van Niekerk, Michael Fanto, Stefan Preble, "Tunable, High Purity Two-Photon Interference From Independent Sources On a Silicon Photonic Chip," IEEE Photonics Conference, TuD3.2, October 2021.
3. Invited Talk / Panelist, NSF Quantum Devices & Systems Manufacturing Workshop, Scaling and Research Community Needs, "300mm Quantum Photonic Wafers," May 26, 2021.
4. Lewis G. Carpenter, Matthew van Niekerk, Amir Begović, Vijay S.S. Sundaram, Venkatesh Deenadayalan, Thomas Palone, Michael Fanto, Stefan Preble, Christopher Baiocco, Gerald L. Leake, Nicholas M. Fahrenkopf, "Towards Low Propagation Losses in Active Photonic Multi-Project Wafer Runs," OSA Advanced Photonics Congress, Advances in Integration Platforms 1, Tu3A, July 2021.
5. Marcel W. Pruessner, Dmitry A. Kozak, Nathan A. Tyndall, William S. Rabinovich, Venkatesh Deenadayalan, Michael Fanto, Stefan Preble, and Todd H. Stievater, "Foundry-processed optomechanical Mach-Zehnder Inteferometers," CLEO – Laser Science to Photonics Applications, Stu2Q.3, May 2021.
6. Gregory Bond, Thomas Palone, Matthew van Niekerk, John Serafini, Mario Ciminelli, Michael Fanto, Stefan F. Preble, "Direct attachment of optical fibers to photonic integrated circuits with in situ UV curing," CLEO: Science and Innovations, JW1A. 29, 2021.
7. Invited Talk, IEEE QCE20 Workshop on Photonic Technologies for Quantum Information Science, "300mm Foundry Fabricated Quantum Photonic Wafer," IEEE International Conference on Quantum Computing and Engineering (QCE20), October 15, 2020.
8. Venkatesh Deenadayalan, Matthew van Niekerk, Michael Fanto, and Stefan Preble, "Ultra-Low Voltage Silicon Photonic MEMS Phase Shifter," IEEE Integrated Photonics Conference 2020 (IPC2020), WD4.6, September 30, 2020.
9. Venkatesh Deenadayalan, Matthew van Niekerk, Michael Fanto, and Stefan Preble, "Silicon Photonic MEMS Phase Shifter Using Gradient Electric Force Actuation," Frontiers in Optics 2020, FW5D.3, September 16, 2020.
10. Matthew van Niekerk, Saman Jahani, Justin Bickford, Pak Cho, Stephen Anderson, Gerald Leake, Daniel Coleman, Michael L. Fanto, Christopher C. Tison, Gregory A. Howland, Zubin Jacob, and Stefan F. Preble, "Demonstration of Two-Dimensional Extreme Skin Depth Engineering in CMOS Photonics Foundry," Frontiers in Optics 2020, FTh1C.5, September 16, 2020.
11. David Starling, Jacob Pourier, Michael Fanto, Jeffrey Steidle, Christopher Tison, Gregory Howland, Stefan Preble, "TM Polarized Photon Pair Generation in Linearly Uncoupled Silicon Resonators," CLEO, FTu4C.2, 2020.

12. Matthew van Niekerk, David J. Starling, Gregory A. Howland, Gerald Leake, Alin Antohe, Siti Binti, Daniel Coleman, A. Matthew Smith, Christopher C. Tison, Michael L. Fanto, Stefan F. Preble, "Experimental Evolutionary Optimization of an Active Multimode Interferometer," CLEO, Jth2B.17, 2020.
13. John Serafini, David Spiecker, Jeffrey Steidle, Michael L. Fanto, Edwin Hach, Stefan Preble, "Two-photon interference via coupled ring resonators on a silicon photonic chip," CLEO, FTu4C.7, 2020.
14. John R Serafini, David Spiecker, Jeffrey A Steidle, Stefan F Preble, Edwin E Hach, Chris C Tisson, Michael L Fanto, Paul M Alsing, Matt Smith, "On-chip demonstration of Hong-Ou-Mandel effect using quantum-optical ring resonators," Quantum Information Science, Sensing, and Computation XI, 10984, 2019.
15. Paul M Thomas, Michael Fanto, John Serafini, Jeffrey Steidle, Stefan Preble, Tsung-Ju Lu, Dirk Englund, "Ion milled facet for direct coupling to optical waveguides," Micro-and Nanotechnology Sensors, Systems, and Applications XI, 10982, 2019.
16. Matthew van Niekerk, Jeffrey A Steidle, Gregory A Howland, Michael L Fanto, Nicholas Soures, Fatima Tuz Zohora, Dhireesha Kudithipudi, Stefan F Preble, "Approximating large scale arbitrary unitaries with integrated multimode interferometers," Quantum Information Science, Sensing, and Computation XI, 10984, 2019.
17. JA Steidle, CC Tison, ML Fanto, SF Preble, PM Alsing, "Highly Directional Silicon Microring Photon Pair Source," CLEO: QELS_Fundamental Science, FTh1D. 4, 2019.
18. Tsung-Ju Lu , Michael Fanto, Hyeongrak Choi, Paul Thomas, Jeffrey Steidle, Sara L. Mouradian, Wei Kong, Di Zhu, Hyowon Moon, Karl K. Berggren, Jeehwan Kim, Mohammad Soltani, Stefan Preble, Dirk . Englund, "An Aluminum Nitride Integrated Photonics Platform for the Ultraviolet to Visible Spectrum," CLEO: Science & Innovations, SF3A.4, 2018, San Jose, California.
19. S. F. Preble, J. A. Steidle, C. C. Tison, M. L. Fanto, P. M. Alsing, "High performance silicon resonator photon sources (Keynote presentation)," Proceedings of SPIE Vol. 10660, Quantum Information Science, Sensing, and Computation X, SPIE Defense + Commercial Sensing, 10660-19.
20. Tsung-Ju Lu, Hyeongrak Choi, Michael Fanto, Jeffrey Steidle, Paul Thomas, Sara Mouradian, Wei Kong, Jeehwan Kim, Stefan Preble, Dirk Englund, "Wide-Bandgap AlN Photonics Platform for Visible to UV Spectrum Quantum Information Processing," MRS Fall Meeting, EM08.03.03, November 28, 2017, Boston, Massachusetts
21. Z. Vernon, M. Menotti, C. Tison, J.A. Steidle, M.L. Fanto, P.M. Thomas, S. F. Preble, G.A. Howland, A.M. Smith, P.M. Alsing, M. Liscidini, J. Sipe, "An Integrated Source of Truly Unentangled Photons for Efficient Single Photon Heralding," Conference on Lasers and Electro-Optics, JTh1E (Optical Society of America, 2017).
22. Jeffrey A. Steidle, Michael L. Fanto, Christopher C. Tison, Zihao Wang, Paul Alsing, Stefan F. Preble, "High Performance Photon Sources for Quantum Silicon Photonics," Frontiers in Optics 2016.
23. S. Preble, J. Steidle, M. Fanto, C. Tison, G. Howland, E. Hach, P. Alsing, "Invited: Quantum Silicon Photonics: Photon sources and Circuits," Frontiers in Optics 2016.

24. Jeffrey A Steidle, Michael L Fanto, Christopher C Tison, Zihao Wang, Paul M Alsing, Stefan F Preble, “Efficiently heralded silicon ring resonator photon-pair source,” Proc. SPIE 9873, Quantum Information and Computation IX, 987304 (May 19, 2016).

Foundry-processed optomechanical photonic integrated circuits: Photonic integrated circuits (PICs) are a maturing technology with foundries enabling wafer-scale PIC fabrication. At the same time, optomechanics, in which micro-/nano-optical and -mechanical structures are coupled, is well-established with many basic research and practical applications. However, optomechanical devices have so far required highly-customized fabrication that limits their inclusion in foundry-processed PICs. To address this need, we design optomechanical PICs using standard low-loss process design kit (PDK) components. Our approach ensures access to the foundry's low-loss PDK components and enables process compatibility. As a demonstration, we design a foundry-processed optomechanical Mach-Zehnder interferometer (MZI). Measurements demonstrate that a π-phase shift can be accumulated over an optomechanical interaction length of only 60 μm and tunable phase shifting can be achieved using gradient electric force actuation. We further demonstrate all-optical excitation and readout of mechanical resonances for sensing applications. Our PDK-focused optomechanics design approach enables the co-integration of optomechanics, photonics, and electronics in a single PIC.

Two-dimensional extreme skin depth engineering for CMOS photonics: Extreme skin depth engineering (e-skid) can be applied to integrated photonics to manipulate the evanescent field of a waveguide. Here we demonstrate that e-skid can be implemented in two directions in order to deterministically engineer the evanescent wave allowing for dense integration with enhanced functionalities. In particular, by increasing the skin depth, we enable the creation of two-dimensional (2D) e-skid directional couplers with large gaps and operational bandwidth. Here we experimentally validate 2D e-skid for integrated photonics in a complementary metal–oxide semiconductor (CMOS) photonics foundry and demonstrate strong coupling with a gap of 1.44 μm.

Nonlinear Photon Pair Generation in a Highly Dispersive Medium: Photon pair generation in silicon photonic integrated circuits relies on four-wave mixing via the third-order nonlinearity. Due to phase matching requirements and group velocity dispersion, this method has typically required TE-polarized light. Here, we demonstrate TM-polarized photon pair production in linearly uncoupled silicon resonators with more than an order of magnitude greater dispersion than in previous work. We achieve measured rates above 2.8 kHz and a conditional self-correlation of $g^{(2)}(0)=0.044$. This method enables phase matching in dispersive media and paves the way for entanglement generation in silicon photonic devices.

An Aluminum Nitride Integrated Photonics Platform for the Ultraviolet to Visible Spectrum: We demonstrate a wide-bandgap semiconductor photonics platform based on nanocrystalline aluminum nitride (AlN) on sapphire. This photonics platform guides light at low loss from the ultraviolet (UV) to the visible spectrum. We measure ring resonators with intrinsic quality factor (Q) exceeding 170,000 at 638 nm and Q >20,000 down to 369.5 nm, which shows a promising path for low-loss integrated photonics in UV and visible spectrum. This platform opens up new possibilities in integrated quantum optics with trapped ions or atom-like color centers in solids, as well as classical applications including nonlinear optics and on-chip UV-spectroscopy.

The path to increasing the heralding efficiency of integrated photon sources: Silicon ring resonators are used as photon pair sources by taking advantage of silicon's large third order nonlinearity with a process known as spontaneous four wave mixing. These sources are capable

of producing pairs of indistinguishable photons but typically suffer from an effective 50% loss. By slightly decoupling the input waveguide from the ring, the desired photons generated in the ring can preferentially be directed to the drop port. Thus, the ratio between the coincidences from the drop port and the total number of coincidences from all ports (coincidence efficiency) can be significantly increased, with the trade-off being that the pump is less efficiently coupled into the ring. In this paper, ring resonators with this design have been demonstrated having coincidence efficiency of ~ 96% but requiring a factor of ~ 10 increase in the pump power. Through the modification of the coupling design that relies on additional spectral dependence, it is possible to achieve similar coincidence efficiencies without the increased pumping requirement. This can be achieved by coupling the input waveguide to the ring multiple times, thus creating a Mach-Zehnder interferometer. This coupler design can be used on both sides of the ring resonator so that resonances supported by one of the couplers are suppressed by the other. This is the ideal configuration for a photon-pair source as it can only support the pump photons at the input side while only allowing the generated photons to leave through the output side. This work realizes a device with preliminary results exhibiting the desired spectral dependence and with a coincidence efficiency as high as ~ 97% while allowing the pump to be nearly critically coupled to the ring. The coincidence efficiency is measured to be near unity and reflects a significant reduction in the intrinsic losses typically associated with double bus resonators This device has the potential to greatly improve the scalability and performance of quantum computing and communication systems.

Truly unentangled photon pairs without spectral filtering: We demonstrate that an integrated silicon microring resonator is capable of efficiently producing photon pairs that are completely unentangled; such pairs are a key component of heralded single-photon sources. A dual-channel interferometric coupling scheme can be used to independently tune the quality factors associated with the pump and signal and idler modes, yielding a biphoton wavefunction with a Schmidt number arbitrarily close to unity. This will permit the generation of heralded single-photon states with unit purity.

Measurement of Quantum Interference in a Silicon Ring-Resonator Photon Source: Silicon photonic chips have the potential to realize complex integrated quantum information processing circuits, including photon sources, qubit manipulation, and integrated single-photon detectors. Here, we present the key aspects of preparing and testing a silicon photonic quantum chip with an integrated photon source and two-photon interferometer. The most important aspect of an integrated quantum circuit is minimizing loss so that all of the generated photons are detected with the highest possible fidelity. Here, we describe how to perform low-loss edge coupling by using an ultra-high numerical aperture fiber to closely match the mode of the silicon waveguides. By using an optimized fusion splicing recipe, the UHNA fiber is seamlessly interfaced with a standard single-mode fiber. This low-loss coupling allows the measurement of high-fidelity photon production in an integrated silicon ring resonator and the subsequent two-photon interference of the produced photons in a closely integrated Mach-Zehnder interferometer. This paper describes the essential procedures for the preparation and characterization of high-performance and scalable silicon quantum photonic circuits.

LIST OF SYMBOLS, ABBREVIATIONS, AND ACRONYMS

AIM Photonics	American Institute for Manufacturing Photonics
AlN	Aluminum Nitride
AFRL	Air Force Research Laboratory
CAR	Coincidental-to-Accidental Ratio
CW	Continuous Wave
DAQ	Data Acquisition
DoD	Department of Defense
FDTD	Finite-Difference Time-Domain
FPGA	Field Programmable Gate Array
FWHM	Full-Width at Half-Maximum
HOM	Hong-Ou-Mandel
MEMS	Micro-electro-mechanical Systems
mW	milliwatt
MZI	Mach-Zehnder Interferometer
N00N	Quantum superposition state |N0> + |0N>
PCB	Printed Circuit Board
PDK	Process Design Kit
PIC	Photonic Integrated Circuit
QPP	Quantum Programmable Processor
RIT	Rochester Institute of Technology
SEM	Scanning Electron Microscope
SFWM	Spontaneous Four Wave Mixing
SiN	Silicon Nitride
SMF	Single Mode Fiber
SPDC	Spontaneous Parametric Down Conversions
TE	Transverse Electric
TM	Transverse Magnetic
UHNA	Ultra-High Numerical Aperture (Fiber)